

THE VIRIAL BALANCE OF CLUMPS AND CORES IN MOLECULAR CLOUDS

SAMI DIB¹, ENRIQUE VÁZQUEZ-SEMADENI¹, JONGSOO KIM², ANDREAS BURKERT³, AND MOHSEN SHADMEHRI⁴

Draft version December 2, 2024

ABSTRACT

We study the virial balance of clumps and cores (CCs) in a set of three-dimensional numerical simulations of driven, magnetohydrodynamical, isothermal molecular clouds (MCs). The simulations represent a range of magnetic field strengths in MCs from subcritical to non-magnetic regimes. We apply a clump finding algorithm based on a density threshold and a friend-of-friend approach to identify independent CCs at the different thresholds level in the simulation box. For each object, we calculate all the terms that enter the virial theorem in its Eulerian form (EVT). We also calculate, for each object, other quantities commonly used in observational and theoretical work to indicate the state of gravitational binding such as the Jeans number J_c , the mass-to magnetic flux ratio μ_c , and the virial parameter α_{vir} . Our results suggest that a) CCs are dynamical out-of-equilibrium structures. b) The surface energy terms are of the same order than their respective volume energy terms and thus are very important in determining the exact energy balance in CCs. c) Clumps can be either in the process of being compressed by the velocity field and have $\tau_k > 0$ or of being dispersed ($\tau_k < 0$). Yet, not all clumps that have $\tau_k > 0$ are necessarily gravitationally bound. d) There is no one-to-one correspondence between the state of the gravitational boundedness of a CC as described by the energy balance analysis (EBA) (i.e., gravity versus other energies) or as implied by the classical indicators J_c , μ_c , and α_{vir} . In general, from the EBA we observe that only the inner regions of the clumps (i.e., the dense cores selected at high density thresholds) are gravitationally bound, whereas J_c and α_{vir} estimates of the same objects tend to show that they are more gravitationally bound at the lowest threshold levels. Additionally, the α_{vir} values indicate a larger number of gravitationally bound objects than what is yielded by the EBA. g) We observe, in the non-magnetic simulation, the existence of a bound core with all the structural and dynamical characteristics of the Barnard 68 Bok globule (B68). This suggests that B68 like cores can form in a larger molecular cloud and then be confined by the warm or hot gas of a newly formed H II region or supernovae explosion, which can heat and rarefy the gas around the core, confine it, and extend its lifetime.

Subject headings: ISM : clouds – ISM : globules – ISM : kinematics and dynamics – ISM : magnetic fields – turbulence – MHD

1. INTRODUCTION

Long standing questions in the process of star formation are the formation mechanisms, structure, and evolution of molecular clouds (MCs) and their substructure of clumps and cores (CCs), which are prone to star formation (e.g., Mouschovias 1995; McKee 1999; Williams et al. 2000; Vázquez-Semadeni et al. 2000; Mac low & Klessen 2004; Elmegreen & Scalo 2004; Ballesteros-Paredes et al. 2006; Burkert 2006). In MCs, which are observed to be turbulent (e.g., Zuckerman & Evans 1974; Zuckerman & Palmer 1974; Larson 1981; Blitz 1993; Williams et al. 2000; Engargiola et al. 2003; Rosolowsky & Blitz 2005; Koda et al. 2006) and magnetized (Heiles et al. 1993; Crutcher 1999; Crutcher et al. 2004), it is essential to understand how the fragmentation process occurs. This is the necessary step on the way to understanding some of the most important results of the star formation process, a) the star formation efficiency

(SFE), both locally in clouds and globally on galactic scales b) Stellar multiplicity and c) The origin of the Initial Mass Function (IMF) and its relationship with the prestellar cores mass distribution (CMD). In the last few decades, several theoretical models have been conceived in order to describe the evolving structure of MCs and there has been a debate on whether MCs and their substructure of CCs are dynamical out-of-equilibrium structures or if they evolve in a state of quasi hydrostatic or magneto-static equilibrium (e.g., Mac Low & Klessen 2004; Mouschovias et al. 2006; Ballesteros-Paredes et al. 2006).

There are two major classes of analytical models used to describe the evolving structure of MCs cores, concentrated around non-magnetic and magnetic configurations. In the non-magnetic case, Jeans (1902) derived the critical mass (i.e., the Jeans Mass) beyond which a system becomes gravitationally unstable against the support provided by the gas thermal motions. This analysis has been expended to include the support provided by isotropic, micro-turbulent motions (von Weizsäcker 1943,1951; Chandrasekhar 1951a,b; Sasao 1973). Since it was soon recognized that molecular clouds are also turbulent on large scales of the order of their own size (e.g., Larson 1981; Ossenkopf & Mac Low 2002), the assumption of micro-turbulence was replaced by turbulent motions that are scale dependent (e.g., Bonazzola et al.

¹ Centro de Radioastronomía y Astrofísica, UNAM, Apdo. 72-3 (Xangari), 58089 Morelia, Michoacán, Mexico; s.dib@astrosmo.unam.mx, e.vazquez@astrosmo.unam.mx

² Korea Astronomy and Space Science Institute, 61-1, Hwaam-dong, Yuseong-gu, Daejeon 305-764, Korea; jskim@kasi.re.kr

³ University Observatory Munich, Scheinerstrasse 1, D-81679 Munich, Germany; burkert@usm.uni-muenchen.de

⁴ Department of Physics, School of Science, Ferdowsi University, Mashhad, Iran; mshadmehri@science1.um.ac.ir

1987; Vázquez-Semadeni & Gazol 1995). In this class of non-magnetic equilibrium configurations, Bonnor (1956) and Ebert (1955,1957) derived analytical solutions for the equilibrium of radial density perturbations in a self-gravitating, isothermal ideal gas and which are solutions of the Lane-Emden equation (Lane 1870; Emden 1907). Column density observations show that the azimuthally averaged, radial density profiles of MCs cores have nearly flat or slow decreasing density in the inner parts and a surrounding envelope with a steeper density gradient (Ward-Thompson et al. 1994,1999; André et al. 1996; Bacmann et al. 2000; Shirley et al. 2000,2002; Evans et al. 2001; Caselli et al. 2002; Young et al. 2003; Keto et al. 2004). Bonnor-Ebert (BE) sphere models have been applied to radial column density profiles observations of dense (average density of $\sim 10^4 - 10^6 \text{ cm}^{-3}$) and cold ($T \sim 10 \text{ K}$) cores (Bacmann et al. 2000; Johnstone et al. 2000; Alves et al. 2001; Evans et al. 2001; Harvey et al. 2001,2003a,b; Racca et al. 2002; Tafalla et al. 2004; Lada et al. 2004; Kirk et al. 2005; Kandori et al. 2005) and the dynamical evolution of BE spheres has been modeled numerically (McLaughlin & Pudritz 1996; Ogino et al. 1999; Keto & Field 2005; Aikawa et al. 2005). A study of isothermal cores whose structure is a solution to the Lane-Emden equation and which are embedded in a larger filamentary structure have been performed by Curry (2000).

The good agreement in some cases between the models and the observational data has led to the assumption that some cores are indeed BE equilibrium configurations, despite the fact that they have, in general, an obvious non-spherical morphology (e.g., Barnard 68; it should be noted however that Lombardi & Bertin 2001, showed that the BE instability is more related to the core's density contrast than to its shape). Ballesteros-Paredes et al. (2003) showed that azimuthally averaged column densities of dynamical, out-of-equilibrium cores formed in a turbulent, isothermal cloud, can be fitted by BE equilibrium profiles. Steinacker et al. (2004) argued that projection effects can be misleading about the true nature of the density distribution of MCs cores. Recently, Keto & Field (2005) and Keto et al. (2006) argued that, not only the density profiles, but also the asymmetric molecular spectral lines observations in some cores (e.g., Ba 68, Lada et al. 2003; Redman et al. 2006) can be explained by non-radial oscillations around an equilibrium BE sphere (see also Galli 2005). An intriguing point about BE spheres models is that, as the volume of the core decreases and central density and density contrast increases, external pressure should increase (e.g., Figs 1, 2, and 3 in Keto & Field 2005). Yet the derived values of external pressures, precisely from BE modeling of cores, by Kandori et al. (2005) do not show this effect (Fig. 7f in their paper). Rather, the external pressure they obtain for a sample of cores which are supposed to represent an evolutionary stage of equilibrium BE spheres, seems to be independent from the density contrast.

A second class of models, introduces magnetic fields as an additional supporting mechanism against gravity (e.g., Mouschovias 1976a,b; Mouschovias 1987; Basu & Mouschovias 1994,1995a,b; Shu et al. 1987). In the framework of this theory, magneto-statically supported cores, which can also account for thermal and micro-turbulent support, (e.g., Lizano & Shu 1989; McLaughlin

& Pudritz 1996), increase their masses by accreting neutrals that drift across the field lines from the surroundings onto the core's surface. This process is called ambipolar diffusion (AD, Mestel & Spitzer 1956). AD will hence tend to increase the mass-to magnetic flux ratio in the core until it becomes larger than a certain critical value allowing for the denser inner parts of the core to collapse gravitationally. Whereas there is no doubt that AD can play an important role provided the ionization fraction inside MCs cores is small, the debate has concentrated on whether AD, which acts on its own timescale of $t_{AD} \sim 10 t_{ff}$ (Fiedler & Mouschovias 1992; Ciolek & Basu 2001), where t_{ff} is the free fall time, has time to play any role at all or whether dense cores which form in convergent flows in turbulent MCs proceed directly to collapse if their gravitational energy dominates all other forms of support (Mouschovias et al. 2006 and references therein; Mac Low & Klessen 2004). On the other hand, magnetic field strength measurements in cores, which can help constrain the AD timescale and the mass-to magnetic flux ratio (which is the main parameter in the theory of magnetically mediated star formation) of the cores, suffers from a major uncertainty which is due to the cores morphologies. Whether the cores are spherical or sheet-like structure can lead to an uncertainty by a factor of 1/3 due to their unknown inclinations. Thus, cores that are classified as being magnetically supercritical, could be subcritical (Crutcher et al. 2004). Though observations tend to indicate that most cores are supercritical (Crutcher 1999; Sarma et al. 2000; Bourke et al. 2001; Crutcher & Troland 2003; Crutcher et al. 2004; Mac Low & Klessen 2004), Mouschovias et al. (2004) discuss the possibility that the latter estimates are biased towards the very innermost parts of the cores and that the supercritical cores are embedded in subcritical envelopes in agreement with the predictions of the AD theory (Cortes et al. 2005; Heiles & Crutcher 2005).

Whether magnetic or non-magnetic, analytical models suffer the fact that they apply only to idealized geometries, and neglect the complex interaction of the star forming CCs with their environment. These facts, along with some observational and theoretical evidences that MCs may have lifetimes not longer than their turbulent crossing time and shorter than what would be implied by the AD-theory (e.g., Lee & Myers 1999; Ballesteros-Paredes et al. 1999a; Palla & Stahler 1999; Elmegreen 2000; Hartmann 2001; Hartmann et al. 2001), have prompted the development of mostly isothermal, magnetized and unmagnetized, turbulent or decaying MCs models in order to study the formation, statistics and properties of the dense structures formed within them (e.g., Padoan 1995,2001; Ostriker et al. 1999; Klessen et al. 2000,2001,2005; Smith et al. 2000; Heitsch et al. 2001; Gammie et al. 2003; Bate et al. 2003; Li et al. 2004; Tilley & Pudritz 2004; Clark & Bonnell 2005; Nakamura & Li 2005). The emerging picture from these models is that dense structures (i.e., clumps) form at the stagnation points of convergent turbulent flows with a tendency for the densest structures (i.e., cores) to form at the intersections of filaments in the clumpy distribution.

In this picture of the dynamical evolution of MCs, the dynamical properties and detailed energy balance of the cloud's substructure remains poorly understood. Hunter

& Fleck (1982) showed that the gravitational boundedness of cores can be influenced by the presence of an external velocity field (i.e., a reduction of the Jeans mass). In the context of CCs forming and evolving in a turbulent parent MC, a valuable tool to quantify their energy balance and state of gravitational boundedness is the virial theorem (Chandrasekhar & Fermi 1953; Strittmatter 1963). It has been widely assumed that MCs and their substructure are in virial equilibrium (e.g., de Jong et al. 1980; Shu et al. 1987; Henriksen 1991). This assumption is also widely spread in observational works (e.g., Larson 1981; Myers 1983; Solomon et al. 1987; Myers & Goodman 1988a,b; Goodman et al. 1993), essentially because their observed kinetic, magnetic and gravitational energies are *of the same order of magnitude*. However, the assumption of the virial balance of CCs in MCs have been contested by several authors, particularly for the smallest clouds which are found to be, in general, non self-gravitating (e.g., Carr 1987; Blitz 1987,1993; Maloney 1988,1990; Herbertz et al. 1991; Bertoldi & McKee 1992; Heyer et al. 2001). The observations by Swift et al. (2006) of a newly discovered core in L1551 (L1551 MC) suggest that this core is highly dynamical and its dynamics is not consistent with a slow gravitational contraction. However, it is not completely uncommon to see the detailed virial balance calculated for CCs in the observations (Ward-Thompson et al. 2002;2006). Ward-Thompson et al. (2006) calculated the detailed virial balance for cores B33-SMM1 and B33-SMM2 in the Horsehead nebulae and found them to be out-of-equilibrium and in near virial equilibrium, respectively. Their estimates, however, took into account only the volume energies and neglected the surface terms in the virial theorem.

The aim of this work is to assess, for CCs which form in three-dimensional, isothermal, turbulent, magnetized MCs models, whether they are virialized and to quantify the importance of the different terms in the virial theorem equation. In § 2, we present the virial theorem, discuss the different terms that enter it. The MCs simulations are presented in § 3, and in § 4, the clump-finding algorithm used to identify the CCs in the simulations is presented. Results of the virial analysis for different MC models are described in § 5. In particular, we emphasize on the correspondence between the gravitational boundedness of CCs as diagnosed from their energy balance on one hand, on the other by classical gravitational boundedness indicators such as the Jeans number, the mass-to-magnetic flux ratio, and the virial parameter, commonly used in theoretical and observational works. In § 6, we summarize our results and conclude.

2. THE EULERIAN VIRIAL THEOREM

Cast in its Eulerian form (Parker 1979; McKee & Zweibel 1992; McKee 1999), the virial theorem (EVT), which is nothing else but a re-writing of the momentum equation after it has been dotted by the position vector and integrated over a given volume of interest, has the following expression

$$\frac{1}{2} \ddot{I}_E = 2(E_{th} + E_k - \tau_{th} - \tau_k) + E_m + \tau_m + W - \frac{1}{2} \frac{d\Phi}{dt}, \quad (1)$$

where $I_E = \int_V \rho r^2 dV$ is the moment of inertia of the

object, r is the distance of each point in the object to its center of mass, and V its volume. $E_{th} = \frac{3}{2} \int_V P dV$ is the volume thermal energy, with P being the thermal pressure, $E_k = \frac{1}{2} \int_V m_i v_i^2 dV$ the volume kinetic energy, $E_m = \frac{1}{8\pi} \int_V B^2 dV$ the volume magnetic energy, $\tau_{th} = \frac{1}{2} \oint_S r_i P \hat{n}_i dS$ the surface thermal energy, $\tau_k = \frac{1}{2} \oint_S r_i \rho v_i v_j \hat{n}_j dS$ the surface kinetic energy, and $\tau_m = \oint_S r_i T_{ij} \hat{n}_j dS$ the surface magnetic energy, where T_{ij} is the Maxwell stress tensor which is given by

$$\mathbf{T} = \frac{1}{4\pi} \left(\mathbf{B} \mathbf{B} - \frac{1}{2} B^2 \mathbf{I} \right), \quad (2)$$

where \mathbf{I} is the diagonal identity tensor. The effects of the gravitational field are described by $W = - \int_V \rho r_i (\partial \phi / \partial r_i) dV$, where ϕ is the gravitational potential. This term is not equal to the volume gravitational energy because the gravitational potential contains a contribution from the object (e.g., clump or core), and the potential due to the external distribution of mass around the object (e.g., the parent cloud), such that $\phi = \phi_{object} + \phi_{ext}$. The last term on the right hand side in Eq. 1 is the first time derivative of the flux of moment of inertia through the boundary of the cloud, $\Phi = \oint_S \rho x^2 v_i \hat{n}_i dS$. In all the previous quantities, \mathbf{v} is the velocity of a point within the defined object relative to the velocity of center of mass of the object.

Few studies have attempted to evaluate the terms involved in Eq. 1 for CCs formed in a turbulent medium (i.e., for non-isolated clouds). Ballesteros-Paredes & Vázquez-Semadeni (1997) and Ballesteros-Paredes et al. (1999b) evaluated some of the EVT terms in 2D numerical simulations and stressed the importance of the surface term, τ_k . Shadmehri et al. (2002) evaluated the different terms of the EVT in the case of dense structures formed in 3D, MHD simulations with grid resolutions of 100^3 . These studies made the assumption that an object is gravitationally bound if its energy balance is such that $(|W| > |2(E_{th} + E_k - \tau_k - \tau_{th}) + E_m + \tau_m|)$. More recently, Tilley & Pudritz (2004,2006), evaluated the non-time dependent terms in the EVT in 3D simulations. Since the latter authors did not calculate the time dependent terms, they have assumed the following: 1) the $d\Phi/dt$ is negligible; 2) the sign of the second time derivative is fixed by the sign of the remaining terms on the right hand side; 3) a cloud is gravitationally bound if $d^2 I_E / dt^2$ is negative. The latter point is particularly confusing, particularly if $d\Phi/dt$ is not evaluated, and which other studies have shown to be non-negligible (Ballesteros-Paredes & Vázquez-Semadeni 1997; Shadmehri et al. 2002 and this study).

Due to the dual role of the thermal, magnetic and kinetic energies and also the gravitational field, which can both help confine an object or disperse it, we argue that the criterion of gravitational boundedness is not only $|W| > |E_{other}|$, but also $(W + E_{other}) < 0$, where $E_{other} = 2(E_{th} + E_k - \tau_k - \tau_{th}) + E_m + \tau_m$. If $(W + E_{other}) < 0$ but $|W| > |E_{other}|$, the object is confined⁵ by forces other than gravity. Fig. 1 shows, in arbitrary units, a diagram describing the state of gravita-

⁵ When an object is confined, whether by gravity or by other forces, it does not mean it is in a state of hydrostatic or magneto-static equilibrium.

tional boundedness of an object according to the balance of the different energy contributions and which we will apply in the next sections to the identified CCs in our simulations.

3. SIMULATIONS

The 3D numerical simulations analyzed in this paper are described in detail in Vázquez-Semadeni et al. (2005). We use the first 4 simulations summarized in Table 1 of that paper, keeping the same nomenclature for the different runs. Here, we briefly recall their basic features. The ideal MHD equations are solved using a total variation diminishing scheme (TVD), which is a second-order-accurate upwind scheme. Its implementation for isothermal flows is described in detail in Kim et al. (1999). Periodic boundary conditions are used in the three directions. The Poisson equation is solved to account for the self-gravity of the gas using a standard Fourier algorithm. In order to achieve second-order accuracy in time, an update step of the momentum density due to the gravitational force is implemented, as in Truelove et al. (1997). Following the method described in Stone et al. (1998), turbulence is constantly driven in the simulation box and the kinetic energy input rate is adjusted as to maintain a constant specified rms sonic Mach number $M_s = 10$. Kinetic energy is injected at large scales, in the wave number range $k = 1 - 2$.

Several issues pertaining to the set of simulations presented in this paper such as the assumption of isothermality, the neglect of ambipolar diffusion, resolution considerations, and the choice of a driven turbulence regime have been discussed in some detail in Vázquez-Semadeni et al. (2005). We complement this discussion by justifying our selection of simulations where turbulence is driven on the largest scales. Our motivation for analyzing such simulations is due to the increased evidence from recent theoretical work and observations that turbulence is most likely driven on large scales in the interstellar medium of different galaxies (Stanimirović & Lazarian 2001 for the LMC; Dib & Burkert 2004, 2005 for Holmberg II; Koda et al. 2006 in the Galaxy). An analysis of the turbulent velocity structure by Ossenkopf & Mac Low (2002) and the filamentary density structure in Taurus by Hartmann (2002) also suggest that MCs are driven on scales which are of the order of their own size, or larger.

The nature of the large scale turbulence driver(s) in the ISM remains an unresolved issue. A minimum level of turbulence might be due to supernova explosions (e.g., Dib et al. 2006), but several large scale instabilities are suspected to play an additional role in that respect, such as instabilities that occur in spiral shocks (Wada & Koda 2004; Bonnell et al. 2005), large scale, gravitational and thermal instabilities (e.g., Wada et al. 2002; Dib & Burkert 2005), generic convergent flows (Heitsch et al. 2005; Audit & Hennebelle 2005; Vázquez-Semadeni et al. 2006) and the magneto-rotational instability (e.g., Selwood & Balbus 1999; Piontek & Ostriker 2005).

When applying a virial balance analysis to CCs in simulations such as ours, a crucial question is: until which time in the evolution of the simulation does the analysis remain valid. Due to the limited numerical resolution, the internal dynamics of a collapsing object can not be accurately followed if the mass of the object exceeds a Jeans mass and if it is not resolved by at least 4 cells in

one direction (Truelove 1997). This criterion translates into a maximum density, which when reached locally in one cell, indicates that the advection of the flow around this cell is numerically biased. Because we are precisely interested in this work in the internal dynamics of the dense structures forming in MCs, we choose to present the detailed analysis only for time-steps which precede the appearance of any collapsed structure in the simulation box. Fig. 2 in Vázquez-Semadeni et al. (2005) shows the evolution of the maximum density in the sample of simulations we analyze in this paper. This figure shows that with a decreasing initial magnetic field, CCs tend to proceed towards collapse at earlier epochs. It should be mentioned though that any selection of CCs in order to investigate their statistics remains valid with the exception that it does not properly describe the internal dynamics of the population of cores which is gravitationally collapsing.

4. SIMULATIONS ANALYSIS

4.1. Clump-finding algorithm

We developed a clump-finding algorithm that is based on a density threshold criterion and a friend-of-friend approach. The clump finding proceeds as follows: cells that have a density higher than the density threshold are selected. Among the selected cells, the maximum is sorted out and all cells spatially connected to it are saved in a separate list that defines the first clump. The density in the first clump cells are then assigned a value close to zero and the second maximum is searched for in the data cube and the procedure is repeated until all cells that define the second clump are found. This is repeated until all cells that have densities higher than the selected density threshold are assigned to a clump. Since our simulations use periodic boundary conditions, the algorithm also checks for clumps that extend across the boundaries of the box. Once the cells of each clump are defined, it becomes easy to calculate, for each clump, all the physical quantities that enter the EVT, in addition to other physical quantities that characterize its structure and dynamics such as its mass M_c , volume V_c , average density \bar{n}_c , velocity dispersion σ_c , and angular momentum J_c . The density thresholds n_{thr} used to define the CCs are, in units of the average density (i.e., $\bar{n} = 500 \text{ cm}^{-3}$), 7.5, 15, 30, 60, and $100 \bar{n}^6$. A few time-steps in some runs have additional clumps determined with thresholds of $500 \bar{n}$. The latter range of density thresholds mimics a large range of critical densities that are necessary to excite various molecular lines in real MCs.

In order to lower numerical noise, we transform the surface terms in the EVT into volume integrals using the Gauss theorem (i.e., $\oint_S \vec{X} d\vec{S} = \int_V \vec{\nabla} \cdot \vec{X} dV$)⁷. The volume integrals are replaced by summations running over all cells belonging to each clump. The time derivatives appearing in Eq. 1 are calculated by assuming that the

⁶ In the figures shown later, different symbols are used to discriminate between the different thresholds. Namely, the 7.5 \bar{n} threshold level is shown with a (+), the 15 \bar{n} with a (*), the 30 \bar{n} with a (◊), the 60 \bar{n} level with a (Δ), and the 100 \bar{n} level with a (□).

⁷ We calculate the x-direction component of the gradient of a quantity A at position (i,j,k) as being $(A(i+1, j, k) - A(i-1, j, k))/2$. The components in the y and z directions are calculated in a similar way.

clump or core, within a time lapse dt , has moved over small distances $d\mathbf{r} = \mathbf{v}_{\text{CM}} \times dt$ following a linear translation (i.e, no acceleration), where \mathbf{v}_{CM} is the velocity of the center of mass of the clump at instant t . Since we can not control \mathbf{v}_{CM} of each object, we use the smallest time separation of time-dumps that is available to us and which amounts to $dt = 0.002 t_s$, where t_s is the simulation box crossing timescale. Thus, the second time derivative of the moment of inertia is calculated using estimates of I_E at three different time-steps $t-dt$, t , and $t+dt$. The flux of moment of inertia $d\Phi/dt$ is an average of the two values calculated from the three consecutive time-steps. The typical shifts in one direction are of the order of 1-2 cells, never exceeding 4 cells. Since the shifts in position associated to shifts from time-step t to time-steps $t-dt$ and $t+dt$ generally correspond to non-integer values, the physical quantities at the shifted time-steps are obtained by using a trilinear interpolation at the new position using all neighboring cells to this new position in the three directions. Hence, the approximation we make is that the volume of the cloud V_c , moves as a rigid body on distances equal to $d\mathbf{r} = \mathbf{v}_{\text{CM}} \times dt$ around the central time-step t . This amounts to applying a Galilean transformation to each core, thus preserving the Eulerian nature of the virial theorem.

In order to check the accuracy of our clump-finding algorithm for the computation of the different physical quantities, the program was tested against a simplified, albeit unphysical, test case problem, consisting of a uniform-density sphere with a pure radial dependence for both the velocity and magnetic fields. The values of the density and the amplitudes of the velocity and magnetic field are arbitrary. The sphere is placed on a uniform, lower density grid with a specified resolution. Fig. 2 shows, in percent, the discrepancy between the analytical solution for each of the physical quantities involved in the EVT and the numerical solution yielded by our algorithm as a function of the number of grid cells present in the diameter of the test sphere. As seen in Fig. 2, 32 cells in each direction are needed in order to bring the uncertainties below the one percent level. Nevertheless, with more than 4 cells per direction, the errors on the EVT quantities are not larger than ~ 15 percent. It should be stressed though, that the relative errors shown in Fig. 2 are only order of magnitude error estimates on the quantities implied in the EVT, because such uncertainties are model dependent. In the case of clumps that have a complex, non-spherical, morphology, which is the case in our simulations, the uncertainty on the physical quantity will be dominated by the uncertainty in the direction with the lowest number of cells. Nevertheless, in order to stay consistent with the results of Fig. 2, we must keep in mind that cores with small number of cells (typically with less than 3 cells in one direction) can be dominated by numerical noise.

In our evaluation of the EVT terms, we have neglected the role played by the driving force which should also appear on the right-hand side of Eq. 1. As the three random components of the driving force for the whole computational domain have not been stored, it is impossible to recover this information since there is no analytical description of this force. However, we do not expect this omission to be a problem since in the simulations, the driving is performed at the largest scales possible,

while the CCs are structures with a much smaller size, in each direction, than the box size. Therefore, the driving mainly advects the CCs, without greatly impacting their internal dynamics.

4.2. Calculation of the classical stability indicators

For each identified CC, we calculate other quantities commonly used in theoretical and observational work to assess the state of gravitational boundedness of the objects, namely, the Jeans number J_c , the mass-to-magnetic flux ratio μ_c , and the virial parameter α_{vir} . It should be mentioned at this stage that these indicators intrinsically suggest that the thermal, kinetic, and magnetic energies act in support against gravity, making two basic simplification to the virial equation: a) The neglect of the surface terms and b) the assumption that W is equal to the gravitational energy of the clump. The Jeans number is defined as $J_c = R_c/L_J$, where R_c is the characteristic size of the CC, $L_{J,c} = (\pi c_s^2/G\bar{\rho}_c)^{1/2}$ is the mean Jeans length of the CC and c_s the sound speed. The mass-to-magnetic flux ratio (M_c/ϕ_c) is generally expressed in units of the critical value for collapse, calculated, in the linear regime, for a sheet-like structure, $(M/\phi)_{cr} \approx (4\pi^2 G)^{-1/2}$ (Nakano & Nakamura 1978). Krasnopolsky & Gammie (2005) showed that this criterion for magnetic criticality holds for turbulent magnetized clouds in the non-linear regime. In principle, the magnetic flux of a CC should be computed as $\phi_c = \int_{S_b} \mathbf{B} \cdot \mathbf{n} dS$, where \mathbf{B} is the mean magnetic field in the CC and \mathbf{n} is the unit vector normal to a surface S that bisects the CC. In complex geometries such as those of the CCs found in our simulations, S_b is difficult to evaluate, particularly for small non-spherical cores which have a limited number of pixels along one direction. Instead, as in Vázquez-Semadeni et al. (2005), we use a simpler approach by defining $\phi_c = \pi R_c^2 \mathbf{B}$, where R_c is the characteristic CC size. We make the common observational assumption that CCs are spherical and compute R_c as being $(3 V_c/4 \pi)^{1/3}$. Alternatively, one could consider that $R_c = V^{1/3}$, or by making the assumption that CCs are flattened, R_c would be the maximum separation between the position of the center of mass and any point (i.e., cell) in the CC. Fig. 3 shows that not all condensations are flattened and even if some are more flattened than others (e.g., Fig. 11), they are not completely cylindrical objects. The interpretation of J_c and μ_c is that J_c measures if a core is gravitationally unstable with respect to the thermal support (i.e., $J_c > 1$), whereas μ_c measures the importance of the magnetic support against gravity. A core is collapsing when $J_c > 1$ and $\mu_c > 1$, while cores with $J_c > 1$ and $\mu_c < 1$ are gravitationally bound but remain in a stable magneto-static state (under ideal MHD conditions such as the simulations analyzed in this work). Cores with $J_c < 1$ are Jeans stable, regardless of the value of μ_c and are likely to re-disperse due to their internal dynamics or loose their identity in subsequent local compressions and dispersions of the local medium by large scale flows. The virial parameter (also called gravitational parameter) is calculated as

$$\alpha_{vir} = \frac{5 \sigma^2 R_c}{G M_c}, \quad (3)$$

where M_c is the mass of the CC and σ is the one-

dimensional velocity dispersion inside the object, calculated as

$$\sigma^2 = \frac{\sigma_t^2}{3} + c_s^2, \quad (4)$$

where σ_t is the turbulent three-dimensional velocity dispersion. The virial parameter is often used in observational and theoretical studies in order to measure the balance between the CCs self-gravity and their kinetic+thermal energies (e.g., Leung et al. 1982; Magnani et al. 1985; Keto & Myers 1986; Herbertz et al. 1991; Bertoldi & McKee 1992; Falgarone et al. 1992; Dobashi et al. 1996; Yonekura et al. 1997; Kawamura et al. 1998; Tachihara et al. 2000,2002; Heyer et al. 2001; Krumholz & McKee 2005). A CC is assumed to be gravitationally bound if $\alpha_{vir} < 1$. We make the common observational assumption that turbulent motions are isotropic in the CCs and calculate, in Eq.4, the one-dimensional turbulent velocity dispersion as being $\sigma = \sigma_t/3^{1/2}$. Associated to the virial parameter is the concept of virial mass, also commonly used in observational works in order to obtain an estimate of the real mass (e.g., Jijina & Myers 1999; Caselli et al. 2002). The virial mass is defined as $M_{vir} = \alpha_{vir} M_c$. CCs whose measured mass is comparable to the virial mass are usually assumed to be in virial equilibrium (e.g., Caselli et al. 2002).

5. VIRIAL BALANCE OF CLUMPS AND CORES

In this section, we present the results concerning the application of the EVT to our set of simulations using the algorithm described in § 4.1. Tab. 1 summarizes the ensemble of CCs found in each simulation, for different density thresholds and at different selected time-steps. At a given time-step, each CC is assigned a number corresponding to its place in the cumulative sum of CCs at all thresholds (i.e., for example in run M10J4 β .1 at $t = 223$, 23 cores have been found, counting all thresholds. Core number 20 corresponds to the first core found at threshold $n_{thr} = 30 \bar{n}$). Tab. 2 summarizes the numbering of CCs in time-steps which are analyzed in detail in the next sections.

5.1. subcritical cloud

In the subcritical run M10J4 β .01 ($\mu_{box} = 0.9$ and initial magnetic field of 45.8 μ G), CCs are observed to be very transient (see the animation in Vázquez-Semadeni et al. 2005), surviving only for time-spans of $0.01 - 0.075 t_s \sim 0.2 - 1.5$ Myr before being dispersed by their internal dynamics, by large scale flows, or by merging with other clumps, and thus, lose their identity. We choose to evaluate the EVT terms in the subcritical run at time-step 223 corresponding to $t = 8.85$ Myr after the simulation has been started, which is the time at which the most massive clump appears in this run. Fig. 3 displays two-dimensional cuts at the position of the peak density of the most massive object found in the simulation, viewed along the three directions of the computational box. Overlaid on the density map are the projected velocity (right column) and magnetic (left column) field components and density contours which show the extent of the clump when selected at the different density thresholds.

Fig. 4 displays the virial balance for all CCs selected at this time-step at all thresholds, i.e., d^2I/dt^2 vs. the

right hand side (RHS) in Eq. 1. Since Eq. 1 is nothing else but a re-writing of the momentum equation, all points should, theoretically, fall on the equality line. Deviations, which are at most of the order of factor ~ 5 are due to two effects: 1) Discretization errors, due to the limited numbers of cells in the CCs, and 2) the neglect of the contribution from the driving force. A legitimate question is: can the small values of d^2I_E/dt^2 for small CCs be considered and indication of dynamical equilibrium? An alternative view to the fact that d^2I_E/dt^2 and the RHS are of the same order and which answers the latter question is given in Fig. 5. This figure shows that, despite the fact that the moment of inertia of the different CCs spans over ~ 10 orders of magnitude, the temporal rate of change, normalized to its own value, in percent, i.e., $|(dI_E/dt)/I_E|$, changes by less than one order of magnitude, irrespective of their masses or sizes. In fact, *the normalized rate of change of the moment of inertia of the smallest clumps is observed to be larger, thus indicating their more transient nature.* In Fig. 6, we evaluate the relative importance of the time derivative of the flux of moment of inertia, i.e. $1/2(d\Phi/dt)$ of all CCs versus the other terms in the RHS in Eq. 1. This term is observed to be the dominant one for almost all CCs, particularly for the largest ones, and is of the same order of magnitude as d^2I_E/dt^2 (i.e., Fig. 7). This fact implies that $(dI_E/dt) \sim -\Phi$, which in turn implies that the time variation of the moment of inertia of a clump is essentially determined by the flux through the its boundary, which is another indication of the transient nature of CCs formed in the simulations.

The evolution of a CC will be determined by the competition between confining forces (negative energies) on the one hand and dispersive ones on the other hand (positive energies). Figs. 8 a,b,c and d compare the importance of the individual surface energy terms to their volume counterparts, and the total surface and volume energy terms, respectively. In general, the surface and volume energy terms are of the same order of magnitude, yet with scatter around the equality value, particularly for the case of the larger clumps. The difference is more important for the kinetic and magnetic energy pairs than for the thermal one. The origin of the differences in the $E - \tau$ relations is twofold. On the one hand, the scatter among different objects is due to the difference of the thermal pressure, velocity and magnetic field between the surface of the clumps and their interior. Second, for the same object, the difference in the scatter at the different density thresholds is simply the result of the energy profile of that object and the position of the surface with respect to the density peak imposed by the density threshold. The larger differences observed in the kinetic and magnetic energy pairs is due to the anisotropic nature of the kinetic and magnetic surface energy terms and is stronger wherever the velocity or magnetic field do not cross smoothly across the surface of the CC. For example, In Fig. 3, it is possible to observe how the velocity field penetrates the clump's boundaries at the thresholds of $7.5 \bar{n}$ and $15 \bar{n}$ becoming more parallel to the clump surface at the higher thresholds of $30 \bar{n}$, $60 \bar{n}$ and $100 \bar{n}$.

Fig. 9 describes the state of gravitational boundedness of the CCs following the approach given in § 2. Objects 1, 12, 20, 22, and 23 correspond to the same condensation seen at the thresholds of 7.5, 15, 30, 60 and $100 \bar{n}$,

respectively (see Tab.2). At high thresholds (30,60 and 100 \bar{n}), the clump has an ellipsoidal structure, with axis ratios of $\sim 1 : 2$. At the lower thresholds of 15 and 7.5 \bar{n} , the clump is linked by a small bridge to a protuberance to the south which causes its morphology to strongly deviate from an ellipsoidal configuration (the bridge is only on one side and not fully seen in the cut at the position of the peak density). The outer envelope is being dispersed by forces other than gravity ($W_1 + E_{others,1} > 0$ and $|W|_1 < |E_{others,1}|$) causing the clump to be ‘peeled’ from the outside. At the intermediate threshold levels of 15, 30, and 60 \bar{n} , the clump is being confined by forces other than gravity ($W + E_{others} < 0$ and $|W| < |E_{others}|$). Material is being redistributed from the main clump towards the southern condensation; see, in Fig. 3a, the projected velocity field pointing southward in the bridge. The inner part of the condensation observed at the highest threshold level of 100 \bar{n} (i.e., core 23) is seen to be slightly gravitationally bound. However, core 23 has only 141 cells and due to its elongation, is dominated by numerical noise along its minor axis. Therefore, the condensation is essentially not bound by gravity. This is why this object, the most massive that forms in this simulation, does not proceed towards collapse. The condensation corresponding to clumps (3,14), defined at the thresholds of 7.5 and 15 \bar{n} , respectively, is found to be bound by forces other than gravity at the lowest threshold level. This object is a low density clump (i.e., its peak density is 29 \bar{n}) and is very flattened. Figs. 11a,b, and c show density cuts at the position of the clump peak density in the three directions of the box along with the projected velocity field. The velocity field is compressing the object along its smallest dimensions and would it not be for the magnetic support (discussed below), it would end up collapsing into a thin sheet, eventually following the description given in Burkert & Hartmann (2004).

In Fig. 10, we reproduce the data of Fig. 9 but where clumps are cataloged by whether they have $\tau_k > 0$ (triangles), which is an indication of net compressive effect by the velocity field or $\tau_k < 0$ (diamonds), which is indicative of a net dispersive effect by the velocity field. The interesting information in Fig. 10, in addition to the fact that most unbound CCs have $\tau_k < 0$, is that, not all of the CCs that are being globally compressed by the velocity field ($\tau_k > 0$) are necessarily dominated by gravity as is assumed in some studies (e.g., Field et al. 2006).

Figs. 12 and 13 display the values of the Jeans number J_c , the mass-to magnetic flux ratio (normalized to the critical value for collapse) μ_c , and the virial parameter α_{vir} for the ensemble of CCs in this simulation (at $t = 223 = 8.85$ Myr). The J_c and α_{vir} values tend to indicate that the most massive condensation (i.e., clumps 1,12,20,22,23) is gravitationally bound, practically at all threshold levels. The object corresponding to clumps (3,14) is marginally bound ($J_c \lesssim 1$ and $\alpha_{vir} \gtrsim 1$). However, both objects are observed to be magnetically supported ($\mu_c < 1$) at all threshold levels, which is in agreement with EBA analysis of not being gravitationally bound. It is important to note that the α_{vir} estimates (Fig. 13) tend to indicate a larger number of gravitationally bound objects with respect to their true energy balance or J_c estimates. This is the case for the second most massive object in the simulation box (corresponding to clumps 2,13,21 at threshold levels of 7.5,15, and

30 \bar{n}) as well as the object corresponding to clumps (4,15 at threshold levels of 7.5 and 15 \bar{n} , respectively). Fig. 9 indicates that the first object is unbound, whereas the second one is confined by the forces other than gravity. These results tend to suggest that *the assessment of the dominance of self-gravity in a clump or core using virial parameter estimates is at the least dubious and should be used in observational studies with caution*. Nevertheless, a fit to the $\alpha_{vir} - M_c$ data in Fig. 13 yields a relation $\alpha_{vir} \propto M_c^{-0.57 \pm 0.04}$ which is in good agreement with the $\alpha_{vir} - M_c$ relations found by Williams et al. (2000) for CCs in the Rosette and G216-2.5 MCs.

Fig. 14 compares the virial mass M_{vir} to the true mass M_c . Interestingly, the range of masses in which $M_{vir} \sim M_c$ [0.2 – 8] M_\odot is very similar to the one observed in Caselli et al. (2002). This similarity does not imply that the objects found in this mass range are in virial equilibrium, but they merely indicate, on the one hand that our simulations correctly represent real MCs, that there is an approximate equipartition between the volume kinetic+thermal and gravitational energies in that mass range though the objects are dynamically evolving and finally, that if the assumptions made in the observations are applied to the CCs found in the simulations, it is possible to recover similar results. The assumptions are :a) neglect of the surface terms, b) sphericity of the clumps, and, c) isotropy of the turbulent motions inside the CCs.

5.2. Moderate supercritical cloud

We now turn to the moderately supercritical cloud (i.e., run M10J4 β .1, $\mu_{box} = 2.8$). In this simulation, we observe the formation of collapsed objects with high peak densities ($n_{peak} \gtrsim 5000 \bar{n}$) at three distinctive time-steps, i.e., frames 44, 130 and 210, corresponding to the epochs of 1.76, 5.2 and 8.4 Myr after the simulation has been started (see animation in Vázquez-Semadeni et al. 2005). We have analyzed the virial balance of CCs in this simulations at frames 30, 40, 50 and 210 (see Tab. 1). Only at time-steps 30 and 40, which precede gravitational collapse in any core, is the internal dynamics accurately described for all CCs according to the Truelove criterion. The diminishing number of clumps detected at the lower thresholds of 7.5 and 15 \bar{n} in Tab. 1 between frames 30 and 210 clearly shows that clumps are merging to form denser structures. An example is shown in Fig. 15 which displays, at $t = 40 = 1.6$ Myr, the ongoing merger of the two most massive cores in the simulation box at this epoch. The merger of these two condensations leads to the formation of a massive core which proceeds towards gravitational collapse at $\sim t = 44 = 1.76$ Myr.

The detailed virial analysis is similar to one presented for the subcritical cloud. The general conclusions drawn from the earlier case such as the verification of Eq. 1, the importance of the time dependent and surface energy terms in the virial equation, and the more transient nature of the smaller and less dense clumps remain valid for the CCs found in this run. However, it is interesting to investigate the energy balance of the CCs at the onset of the cloud merger observed in Fig. 15. The energy balance of the ensemble of CCs at this epoch is displayed in Fig. 16. The most massive condensation corresponds to clumps 1,17,28,35 at the threshold levels of 7.5,15,30,60 \bar{n} , respectively, and 38 and 39 at the threshold of 100

\bar{n} which are the two merging cores observed in Fig. 15. The condensation as a whole is observed to be non self-gravitating at the lowest thresholds (i.e., clumps 1 and 17) but is in the process of being compressed by the velocity field (i.e., Fig. 17). At higher threshold levels, the condensation is gravitationally bound (clumps 28 and 39) or marginally bound (clumps 35 and 38). On the other hand, the calculated J_c , μ_c , and α_{vir} values for this condensation (i.e., Figs. 18 and 19) suggest that it is gravitationally bound at almost all thresholds (except for core 39 which has $J_{c,39} \lesssim 1$), and close to magnetic criticality ($\mu_c \lesssim 1$)⁸.

In contrast to the subcritical run, a larger number of condensations are observed to be gravitationally bound. The condensation corresponding to clumps (2,18,29 and 36) is observed to be gravitationally bound at all threshold levels and the inner parts of the condensations corresponding to clumps (3,19,30, and 37) are gravitationally bound (cores 30 and 37). Condensation (2,18,29,36), however, is numerically under-resolved with a total number of cells of 43 (i.e., at the lowest threshold) with a thickness of two cells in one direction and thus its energy balance is unreliable according to the rough uncertainty estimates in Fig. 2. Condensation (3,19,30, and 37) is a well resolved object (i.e., 2794 cells at the lowest threshold level of $7.5 \bar{n}$). The EBA analysis tends to indicate that the inner parts of this condensation are more strongly gravitationally bound (i.e., $|W|/|E_{others}|_{37} > |W|/|E_{other}|_{30} > |W|/|E_{other}|_{3,19}$). On the other hand, the classical indicators tend to show that the condensation is more gravitationally bound or marginally bound as a whole than its inner parts as indicated by the α_{vir} and J_c estimates ($\alpha_{vir,3,19} < \alpha_{vir,30} < \alpha_{vir,37}$; $J_{c,3,19} > J_{c,30} > J_{c,37}$) and the fact that the inner parts are less magnetically supported than the condensation as a whole according to the μ_c estimates ($\mu_{c,37} < \mu_{c,30} < \mu_{c,3,19}$).

As in the subcritical cloud case, the α_{vir} estimates tend to indicate a larger number of gravitationally bound CCs than that implied by the EBA and Jeans number estimates. An example is the case of the condensation corresponding to clumps 6,12, and 33 (defined at the $7.5, 15$ and $30 \bar{n}$ threshold levels, respectively) which is seen to be gravitationally bound according to its α_{vir} values (i.e., Fig. 19) whereas Fig. 16 indicates that this condensation is bound by forces other than gravity (outer parts, clumps 6, 22) or unbound (inner parts, core 33). The relationship between the α_{vir} gravitational boundedness estimator and the real mass M_c in Fig. 19 is well fitted by a $\alpha_{vir} \propto M_c^{-0.60 \pm 0.03}$ which is also in good agreement with the $\alpha_{vir} - M_c$ relation in Williams et al. (2000).

5.3. Strongly supercritical cloud

In this section, we discuss the gravitational boundedness of CCs that form in a strongly supercritical cloud M10J4 β 1 (i.e., weak magnetic field of $4.6 \mu\text{G}$ and $m_{box} = 8.8$). A visualization of the time evolution of the dense structures formed in this cloud model (see animation in Vázquez-Semadeni et al. 2005) shows the existence of

⁸ If the characteristic radius of the clumps were calculated as the cubic root of the volume and not as the radius of a sphere of equivalent volume, the magnetic flux would be larger by a factor of ~ 3 and as a result the clumps would be slightly supercritical $\mu_{c,1,17,28,35,38} \gtrsim 1$.

both collapsed, and other, non-collapsing, long-lived condensations. The first of these long-lived condensations appears at time-step $t = 16 = 0.64$ Myr and disperses around frame $t = 84 = 3.36$ Myr. At the epoch at which we perform our analysis (i.e., at time-step $t = 30 = 1.2$ Myr), collapsing object is present in the simulation box. The clump-finding algorithm finds three condensations at all thresholds levels (i.e., $7.5, 15, 30, 60$ and $100 \bar{n}$), namely the condensations corresponding to clumps (1,12,23,32,37), (2,13,24,33,38) and (3,14,25,34,39). Two condensations are observed at the first four threshold levels (i.e., clumps 4,15,26,35 and 5,16,27,36, respectively), and six condensations are observed at lower threshold levels (i.e., Tab. 1).

Fig. 20 shows the energy balance for the ensemble of CCs at the selected time-step. The different condensations show a diverse behavior. The central regions of the condensation that contains the highest density peak (i.e., object 1,12,23,32,37) are observed to be gravitationally bound (i.e., cores 32 and 37) whereas when considered with its larger envelope, it is gravitationally unbound (i.e., objects 1,12, and 23). Similarly to the cases discussed in the previous sections, the values of the classical indicators, J_c , μ_c , and α_{vir} for this condensation suggest that it is bound at all threshold levels, and magnetically more supercritical when considered with its extended envelope (i.e., Figs. 21 and 22). The second condensation (i.e., clumps 2,13,24,33,38) displays a rather complex behavior. The classical indicators suggest that it is gravitationally bound (i.e., α_{vir} estimates in Fig. 22) or marginally bound (i.e., J_c estimates in Fig. 21), whereas its energy balance tends to indicate that it is confined by forces other than gravity (thermal pressure, dynamical compression and the magnetic force). At the second highest threshold level (i.e., $60 \bar{n}$), it is observed to be marginally bound (i.e., core 33, $|W|/|E_{other}| \lesssim 1.5$). This is one of the condensations which are observed to be long lived. The third condensation (i.e., clumps 3,14,25,34, and 39) is found to be gravitationally bound at all threshold levels in the EBA and is one of the objects that later proceeds to gravitational collapse. Another condensation exhibits the same trend as the first two condensations of having a gravitationally bound or marginally bound central region (i.e., cores 26 and 35) and an envelope that is unbound (i.e., clumps 4 and 15).

We note that in this simulation as well, the α_{vir} estimates (Fig. 22) tend to suggest a larger number of gravitationally bound clumps than what is indicated by the EBA. Additionally, the comparison of the real mass to the virial mass (i.e., Fig. 23) would suggest that a large number of clumps in the mass range $[\sim 0.3 - 8] M_\odot$ are in virial equilibrium, in disagreement with their EBA. We also note that the M_{vir} estimates of the objects at the lowest thresholds are larger than those at higher threshold levels. A fact reported by Tachihara et al. (2000) from their ^{13}CO and C^{18}O survey of cores in Ophiuchus. The real mass- α_{vir} relation for the CCs presented in this section is $\alpha_{vir} \propto M^{-0.50 \pm 0.04}$ (i.e., fit over-plotted to the data in Fig. 22) which remains in good agreement with the results of Williams et al (2000).

5.4. Nonmagnetic cloud

In the non-magnetic cloud (i.e., run M10J4 β inf), the clumps are observed to evolve quickly towards gravitational collapse (see Fig. 2 in Vázquez-Semadeni et al. 2005 and the animation therein). At $t = 30 = 1.2$ Myr after the start of the simulation, there are already 5 independent cores whose average density is higher than $500\bar{n}$ (i.e., Tab. 1). We should remind that in our simulations, whenever the density in a cell violates the Truelove criterion (Truelove 1997) and becomes higher than $\sim 256\bar{n}$, the dynamics around this cell becomes numerically unreliable. Therefore, we show the results of the EBA at an earlier epoch (i.e., time-step $t = 20 = 0.8$ Myr), at which only one object has collapsed. Fig. 24 displays the energy balance of CCs at this epoch. The most massive object corresponds to clumps 1,24,47,70,85, and 88 at the thresholds levels of 10,15,30,60,100, and $500\bar{n}$, respectively. The inner regions of this object are observed to be undergoing gravitational collapse (i.e., cores 85 and 88 since e.g., $|W_{88}| \gg |2(E_{k,88} - \tau_{th,88} - \tau_{k,88} - \tau_{th,88})|$) while the object as a whole is found to be unbound (clumps, 1,24,47 and 70). Two other condensations corresponding to clumps 2,25,48,71, and 86 (at thresholds levels of 10,15,30,60, and 100, respectively) and 14,37,60, and 83 (at threshold levels of 10,15,30, and $60\bar{n}$, respectively) are also observed to have a gravitationally bound core (i.e., cores 86 and 83, respectively) and a more dilute, unbound envelope.

A peculiar condensation is the one corresponding to clumps (14,37,60, and 83, at threshold levels 10,15,30, and 60, respectively), which is found to be gravitationally bound at all threshold levels (see Fig. 24). This object is small i.e., 64 cells in total, has 3-5 cells in each direction which correspond to a physical size of 0.046-0.078 pc, has sharp boundaries, an average number density of $\sim 65\bar{n} \sim 3.2 \times 10^4 \text{ cm}^{-3}$ which is nearly-independent of the selected density threshold level, a peak number density of $76.4\bar{n} \sim 4 \times 10^4 \text{ cm}^{-3}$, a mass of $\sim 1.5 M_{\odot}$ and a non-thermal velocity dispersion of 0.036 km s^{-1} . This implies a one-dimensional velocity dispersion of $\sim 0.036/3^{1/2} \sim 0.02 \text{ km s}^{-1}$, which is roughly one tenth of the thermal sound speed. Thus, very interestingly, all of the structural and dynamical properties of this object resemble very closely those of Bok globules and particularly those of the Bok globule Barnard 68 (e.g., Hotzel et al. 2002a,b; Lada et al. 2003). Unfortunately, due to the low numbers of cells available in each direction, it is not possible to draw, for this core, the velocity profile in order to check if they present any of the observational evidence of spatial asymmetry in the blue-shifted and red-shifted components of molecular lines such as the case of B68 (Redman et al. 2006).

One noticeable fact about this non-magnetic cloud simulation is that the number of condensations that are found to be gravitationally bound or readily collapsing is not particularly larger than the number of gravitationally bound objects found in the magnetized runs M10J4 β .1 and M10J4 β . However, though the mass range of CCs in all simulations is roughly the same, the total number of clumps and particularly the number of small clumps is much larger in the non-magnetized cloud than in the magnetized ones (see Tab. 1). Figs. 27 and 28, which display the J_c and α_{vir} estimates in this run, respectively, illustrate this effect; i.e., same mass range of the clumps as

in the magnetized runs but with larger numbers of small size CCs. Therefore, the presence of a magnetic field in the cloud seems to influence the star formation process by essentially reducing the number of formed cores within a certain volume rather by substantially preventing or delaying the collapse process in individual clouds once gravity has overcome all other forces.

Similarly to the cases of the magnetized clouds discussed earlier, the J_c and α_{vir} estimates for the ensemble of CCs in this simulation (i.e., Figs. 27 and 28) suggest that the most massive condensations (condensation 1 corresponding to clumps 1,24,47,70,85 and 88 and condensation 2 corresponding to clumps 2,25,48,71,86) are gravitationally bound at all threshold levels, being also more bound for the cloud as a whole (i.e., when defined at a lower threshold level). This is in disagreement with the EBA analysis which suggests that only the inner regions of these condensations are gravitationally bound. Also, in this non-magnetic case, the α_{vir} estimates would catalog some CCs as being gravitationally bound (e.g., clump 76) or marginally bound (e.g., clump 87), in disagreement with the detailed EBA, which suggests they are not. We find that the $\alpha_{vir} - M_c$ relation (over-plotted to the data in Fig. 28) is $\alpha_{vir} \propto M_c^{-0.47 \pm 0.03}$ which is less steep than the same relation in the magnetized simulations. This suggests that the presence of the magnetic field in the cores modifies both the density profile and the velocity dispersion-radius relations in the cores upon which the value of α_{vir} is dependent. Understanding the exponent of the $\alpha_{vir} - M_c$ relation requires a careful study of the radial density profiles of the cores drawn along their symmetry axis and is left to future detailed study.

After discussing the energy balance in the sample of magnetized and non-magnetized simulations, two additional points are worth mentioning: a) We do not observe, in any of the analyzed simulation, CCs that are positioned in the upper right quadrant in the $(W + E_{other}) - (|W|/|E_{other}|)$ diagrams. This simply means that the extended distribution of mass around the CCs has very little influence on the CCs gravitational boundedness and that the gravitational term W is always close to the CCs gravitational energy; b) We observe that some CCs, which are dynamical in essence, have $W + E_{other} \sim 0$ and $|W|/|E_{other}| \sim 1$ (i.e., Figs. 16 and 20). This could lead them to be cataloged as being in a state of *magneto-static equilibrium*, which is not supported by their virial analysis.

6. CONCLUSIONS AND DISCUSSION

Understanding the gravitational binding of clumps and cores (CCs) in molecular clouds (MCs) is a key element in better describing the process of fragmentation of a cloud which, itself, is the necessary step on the way of better understanding the process of star formation in the dense regions of a MC, the origin of stellar multiplicity, and the initial stellar mass function (see, e.g., Padoan & Nordlund 2002,2004; Mac Low & Klessen 2004; Ballesteros-Paredes et al. 2006; Klein et al. 2006).

In this paper, we have analyzed the virial balance of CCs that form in isothermal, magnetohydrodynamical, driven MCs. The analyzed simulations vary by the strength of the magnetic field initially present in the box ranging from subcritical to non-magnetic regimes. For

each simulation, the selection of the CCs and the virial analysis performed at different time-steps. However, in order to follow more accurately the internal dynamics inside the analyzed CCs, results are preferentially presented at time-steps that precede the appearance of collapsed objects in the simulation box. CCs have been identified by a friend-of-friend algorithm as being an ensemble of connected cells that have a density higher than a defined density threshold. We have used a range of selected thresholds (i.e., from 7.5 to 100 times the average density) that covers a wide dynamical range that mimics the usage of various density tracers sensitive to different average gas densities in the observations. Once an object has been defined, we calculate for this object all the quantities that appear in the virial theorem in its Eulerian form (Eq. 1), along with other quantities such as its mass, volume, average density, internal velocity dispersion and three quantities commonly used as gravitational binding indicators, namely the Jeans number J_c , the mass-to magnetic flux ratio (normalized to the critical value or collapse) μ_c , and the virial parameter α_{vir} . Our results show that :

a) CCs are not in virial equilibrium, and are dynamical out-of-equilibrium structures as indicated by their complex changing geometry over time and the importance of the flux of moment of inertia term in the virial equation, which is a quantitative confirmation of the highly dynamical, morphing nature of clumps in a molecular cloud.

b) The surface energy terms are of the same order than the volume energy term (by up to a factor ~ 5 smaller or larger) and, thus, are very important in determining the energy balance in CCs. Particularly important are the anisotropic kinetic and magnetic surface energy terms, which are related to the complex topology of the velocity and magnetic fields at the defined boundary of the CC. We observe that the difference between the volume and surface term is larger whenever the velocity or magnetic field does not cross smoothly the surface of the object, due for example to the presence of a high density peak.

c) We observe that CCs can be either in the process of being compressed by the velocity field and in that case they have $\tau_k > 0$ or of being dispersed ($\tau_k < 0$). Yet, not all CCs that have $\tau_k > 0$ are necessarily gravitationally bound, but are simply in the process of assembling from less dense gas by turbulent ram pressure.

d) Despite their dynamical nature, some CCs are observed to have $W + E_{other} \sim 0$ and $|W|/|E_{other}| \sim 1$ which can lead them, erroneously, to be cataloged as being in a state of *magneto-static equilibrium*. Additionally, we find, in all simulations, that the gravitational term must always be close to the gravitational energy and that the mass distribution outside the CCs does not have a significant contribution in distorting the CCs structure by external gravitational torques.

e) We have shown that there is no one-to-one correspondence between the state of the gravitational binding of a CC as described by the energy balance anal-

ysis (EBA) (i.e., gravity versus other energies) and as implied by the classical gravitational binding indicators J_c , μ_c , and α_{vir} . In general, from the EBA we observe that only the inner regions of the clumps (i.e., the dense cores selected at high density thresholds) are gravitationally bound, whereas Jeans number estimates of the same clumps tend to show that the objects are gravitationally bound at all threshold levels. On the other hand, the calculated α_{vir} values not only show that the clumps are more gravitationally bound at the lower threshold levels as the Jeans numbers, but also indicate a number of gravitationally bound objects always in excess of what is yielded by the EBA.

f) In the non-magnetic simulations, we have observed the formation of a core which possesses all the structural and dynamical properties of the Bok globule Barnard 68 (B68). This core is gravitationally bound. Such bound cores may survive the ionizing front of a H II region formed elsewhere in the cloud and which expands in the cloud's clumpy distribution (e.g., Mellema et al. 2006; Will Henney, private communication). The ionizing front can evacuate the gas around the core, and leave it confined by a surrounding warm gas such as in the case of B68.

In the set of simulations presented in this work, we have used an isothermal equation of state to describe the gas physics. However, several authors have argued recently that deviations from isothermality in molecular clouds might lead them to have distinct structural and/or dynamical properties than isothermal clouds (Larson 2005). Li et al. (2003) and Jappsen et al. (2004) showed that the fragmentation process is dependent on the polytropic exponent which describes the equation of state. Dib et al. (2004) showed that the average density-size relation for non-isothermal clouds follows the observed $\bar{n} R_c^{-1}$ Larson relations (Larson, 1981) unlike the isothermal clouds and their substructure is which this relation is not found (e.g., Li et al. 2004). Hennebelle & Inutsuka (2006) discuss the possibility that warm gas can survive inside MCs Pavlovski et al. (2006), showed, however, that global deviations from isothermality are only visible in terms of the high temperature zones behind shock waves. The detailed effects of a non-isothermal equation of state on the properties of individual cores has not been investigated in detail so far, and is left to a future work.

S.D. is supported by a UNAM postdoctoral fellowship, E.V.-S. by CONACyT grant 47366-F and J. K. by the Astrophysical Research Center for the Structure and Evolution of the COSMOS (ARCSEC) of the Korea Science and Engineering Foundation through the Science Research Center (SRC) program. The numerical simulations analyzed in this paper were performed on the Linux clusters at KASI, with funding from KASI and ARCSEC, and at CRyA, with funding from CONACyT grant 36571-E. This research has made use of NASA's Astrophysics Data System Bibliographic Services.

REFERENCES

- Aikawa, Y., Herbst, E., Roberts, H., & Caselli, P. 2005, ApJ, 620, 330
 Alves, J. F., Lada, C. J., & Lada, E. A. 2001, Nature, 409, 159
 Alves, J. F., Lada, C. J., & Lada, E. A. 2001, The Messenger, 103, 1
 André, P., Ward-Thompson, D. & Motte, F. 1996, A&A, 314, 625
 Audit, E., & Hennebelle, P. 2005, A&A, 433, 1

- Bacmann, A., André, P., Puget, J.-L., Abergel, A., Bontemps, S., & Ward-Thompson, D. 2000, *A&A*, 361, 555
- Ballesteros-Paredes, J., & Vázquez-Semadeni, E. 1997, *AIP Conf. Series*, 393, 81
- Ballesteros-Paredes, J., Hartmann, L., & Vázquez-Semadeni, E. 1999, *ApJ*, 527, 285
- Ballesteros-Paredes, J., Vázquez-Semadeni, E., & Scalo, J. 1999, *ApJ*, 515, 286
- Ballesteros-Paredes, J., Klessen, R. S., & Vázquez-Semadeni, E. 2003, *ApJ*, 592, 188
- Ballesteros-Paredes, J., Klessen, R. S., Mac Low, M.-M., Vázquez-Semadeni, E. 2006, in *Protostars and Planets V*, ed. B. Reipurth, D. Jewitt, & K. Keil (Tuscon: Univ. Arizona Press)
- Basu, S., Mouschovias, T. Ch., 1994, *ApJ*, 453, 271
- Basu, S., Mouschovias, T. Ch., 1995, *ApJ*, 452, 386
- Basu, S., Mouschovias, T. Ch., 1995, *ApJ*, 453, 271
- Bate, M. R., Bonnell, I. A., & Bromm, V. 2003, *MNRAS*, 339, 577
- Bertoldi, F., & McKee C. F. 1992, *ApJ*, 395, 140
- Blitz, L. 1987, in *Physical Processes in Interstellar Clouds*, ed. G. Morfill & M. Scholer (Dordrecht:Reidel), 35
- Blitz, L. 1993, in *Protostars and Planets III*, ed. E. H. Levy & J. I. Lunine (Tuscon:Univ. Arizona Press), 125
- Bonnell, I. A., Dobbs, C. L., Robitaille, T. R., & Pringle J. E. 2006, *MNRAS*, 365, 37
- Bonnor, W. B. *MNRAS*, 116, 351
- Bonazolla, S. E., Falgarone, E., Heyvarts, J., Perault, M., & Puget, J.-L. 1987, *A&A*, 172, 293
- Bourke, T. L., Myers, P. C., Robinson, G., & Hyland, A. R. 2001, *ApJ*, 554, 916
- Burkert, A., & Hartmann, L. 2004, *ApJ*, 616, 288
- Burkert, A. 2006, in *Statistical Mechanics of Non-Extensive Systems*, ed. F. Combes & R. Robert (Elsevier), astro-ph/0605088
- Carr, J. S. 1987, *ApJ*, 323, 170
- Caselli, P., Benson, P., Myers, P. C., & Tafalla, M. 2002, *ApJ*, 572, 238
- Ciolek, G. E., & Basu, S. 2001, *ApJ*, 547, 272
- Clark, P. C., & Bonnell, I. A. 2005, *ApJ*, 361, 2
- Chandrasekhar, S. 1951, *Proc. R. Soc. London, Ser. A* 210, 18
- Chandrasekhar, S. 1951, *Proc. R. Soc. London, Ser. A* 210, 26
- Chandrasekhar, S. & Fermi, E. 1953, *ApJ*, 118, 116
- Cortes, P. C., Crutcher, R. M., & Watson, W. D. 2005, *ApJ*, 628, 780
- Crutcher, R. M. 1999, *ApJ*, 520, 706
- Crutcher, R. M., & Troland, T. H. 2000, *ApJ*, 537, L139
- Crutcher, R. M., Nutter, D., J., Ward-Thompson, D., & Kirk J. M. 2004, 600, 279
- Curry, C. L. 2000, *ApJ*, 541, 831
- de Jong, T., Boland, W., & Dalgarno, A. 1980, *A&A*, 91, 68
- Dib, S., & Burkert, A. 2004, *Ap&SS*, 292, 135
- Dib, S., Burkert, A. & Hujeriat, A. 2004, *Ap&SS*, 289, 465
- Dib, S., & Burkert, A. 2005, *ApJ*, 630, 238
- Dib, S., Bell, E., & Burkert, A. 2006, *ApJ*, 638, 797
- Dobashi, K., Bernard, J. P., & Fukui, Y. 1996, *ApJ*, 466, 282
- Ebert, R. 1955, *Z. Astrophys.*, 36, 222
- Ebert, R. 1957, *Z. Astrophys.*, 42, 263
- Elmegreen, B. G. 2000, *ApJ*, 530, 277
- Elmegreen, B., & Scalo, J. 2004, *ARA&A*, 42, 211
- Engargiola, G., Plambeck, R. L., Rosolowsky, E., & Blitz, L. 2003, *ApJS*, 149, 343
- Evans, N. J., Rawlings, J. M. C., Shirley, Y. L., & Mundy, L. G. 2001, *ApJ*, 557, 193
- Falgarone, E., Puget, J.-L., & Perault, M. 1992, *A&A*, 275, 715
- Fiedler, R. A., & Mouschovias, T. Ch. 1992, *ApJ*, 391, 199
- Field, G. B., Blackman, E. G., & Keto, E. 2006, *ApJL*, submitted, (astro-ph/0601574)
- Fuller, G. A., & Myers, P. C. 1992, *ApJ*, 384, 523
- Galli, D. 2005, *MNRAS*, 359, 1083
- Gammie, C. F., Lin, Y.-T., Stone, J., M., & Ostriker, E. C. 2003, *ApJ*, 592, 203
- Goodman, A. A., Benson, P. J., Fuller, G. A., & Myers, P. C. 1993, *ApJ*, 406, 528
- Hartmann, L. 2001, *AJ*, 121, 1030
- Hartmann, L. 2002, *ApJ*, 578, 914
- Hartmann, L., Ballesteros-Paredes, J., & Bergin, E. A. 2001, *ApJ*, 562, 852
- Harvey, D. W. A., Wilner, D. J., Lada, C. J., Myers, P. C., Alves, J. F., & Chen, H. 2001, *ApJ*, 563, 903
- Harvey, D. W. A., Wilner, D. J., Myers, P. C., & Tafalla, M. 2003, *ApJ*, 597, 424
- Harvey, D. W. A., Wilner, D. J., Lada, C. J., Myers, P. C., & Alves, J. F. 2003, *ApJ*, 598, 1112
- Heiles, C., Goodman, A., McKee, C. F. & Zweibel, E. G. 1993, in *protostars and planets III*, ed. E. H. Levy & J. I. Lunine (Tuscon: Univ. Arizona Press), 279
- Heiles, C. & Crutcher, R. M. 2005, (astro-ph/0501550)
- Heitsch, F., Mac Low, M.-M., & Klessen, R. S. 2001, *ApJ*, 547, 280
- Heitsch, F., Burkert, A., Hartmann, L. W., Slyz, A. D., & Devriendt, J. E. G. 2005, *ApJ*, 633, L133
- Hennabelle, P., Inutsuka, S., 2006, *ApJ*, accepted, (astro-ph/0510389)
- Henriksen, R. N. 1991, *ApJ*, 377, 500
- Herbertz, R., Ungerechts, H., & Winnewisser, G. 1991, *A&A*, 249, 483
- Heyer, M. H., Carpenter, J. M., & Snell, R. L. 2001, *ApJ*, 551, 852
- Hotzel, S., Harju, J., Juvela, M., Mattila, K., & Haikala, L. K. 2002, *A&A*, 391, 275
- Hotzel, S., Harju, J., & Juvela, M. 2002, *A&A*, 395, 5
- Hunter, J. H. JR., & Fleck, R. C. JR. 1982, *ApJ*, 256, 505
- Jappsen, A.-K., Klessen, R. S., Larson, R. B., Li, Y. & Mac Low, M.-M. 2005, *A&A*, 435, 611
- Jeans, J. H. 1902, *Philos. Trans. R. Soc. London, Ser. A* 199, 1
- Jijina, J., Myers, P. C., & Adams, F. C. 1999, *ApJS*, 125, 161
- Johnstone, D., Wilson, C. D. Moriarty-Schieven, G., Joncas, G., Smith, G., Gregersen, E., & Fich, M. 2000, *ApJ*, 545, 327
- Kandori, R., Nakajima, Y., Tamura, M., Tatematsu, K., Aikawa, Y., Naoi, T., Sugitani, K., Nakaya, H., Nagayama, T., Nagata, T., Kurita, M., Kato, D., Nagashima, C., & Sato, S. 2005, *AJ*, 130, 216
- Kawamura, A., Onishi, T., Yonekura, Y., Dobashi, K., Mizuno, A., Ogawa, H., & Fukui, Y. 1998, *ApJS*, 117, 387
- Keto, E., & Myers, P. C. 1986, *ApJ*, 304, 466
- Keto, E., Rybicki, G. B., Bergin, E. A., & Plume, R. 2004, *ApJ*, 613, 355
- Keto, E., & Field, G. 2005, *ApJ*, 635, 1151
- Keto, E., Broderick, A., Lada, C. J., & Narayan, R. 2006, *ApJ*, submitted, (astro-ph/0602262)
- Kim, J., Ryu, D., Jones, T. W., & Hong, S. S. 1999, *ApJ*, 514, 506
- Kirk, J. M., Ward-Thompson, D., & André, P. 2005, *MNRAS*, 360, 1506
- Klein, R. I., Inutsuka, S.-I., Padoan, P., & Tomisaka, K. 2006, in *Protostars and Planets V*, ed. B. Reipurth, D. Jewitt, & K. Keil (Tuscon: Univ. Arizona Press)
- Klessen, R. S., Heitsch, F., & Mac Low, M.-M. 2000, *ApJ*, 535, 887
- Klessen, R. S. 2001, *ApJ*, 556, 837
- Klessen, R. S., Ballesteros-Paredes, J., Vázquez-Semadeni, E., & Durán-Rojas, C. 2005, *ApJ*, 620, 786
- Koda, J., Sawada, T., Hasegawa, T. & Scoville, N. Z. 2006, *ApJ*, 638, 191
- Krasnopolsky, R., & Gammie, C. F. 2005, *ApJ*, 635, 1126
- Krumholz, M. R., & McKee, C. F. 2005, *ApJ*, 630, 250
- Lada, C. J., Bergin, E. A., Alves, J. F. & Huard, T. L. 2003, *ApJ*, 586, 286
- Lada, C. J., Huard, T. L., Crews, L. J., & Alves, J. F. 2004, *ApJ*, 610, 303
- Larson, R. B. 1981, *MNRAS*, 194, 809
- Larson, R., B. 2005, *MNRAS*, 359, 211
- Lee, C. W., & Myers, P. C. 1999, *ApJS*, 123, 233
- Leung, C. M., Kutner, M., L., & Mead, K. N. 1982, *ApJ*, 262, 583
- Li, Y., Klessen, R. S., & Mac Low, M.-M. 2003, *ApJ*, 592, 975
- Li, P. S., Norman, M. L., Mac Low, M.-M., & Heitsch, F. 2004, *ApJ*, 605, 800
- Lizano, S., & Shu, F. H. 1989, *apj*, 342, 834
- Lombardi, M., & Bertin, G. 2001, *A&A*, 375, 1091
- Mac Low, M.-M., & Klessen, R. S. 2004, *Rev. Mod. Phys.*, 76, 125
- Magnani, L., Blitz, L., & Mundy, L. 1985, *ApJ*, 295, 402
- Maloney, P. 1988, *ApJ*, 334, 761
- Maloney, P. 1990, *ApJ*, 348, 9
- McKee, C. F., & Zweibel, E. G. 1992, *ApJ*, 399, 551
- McKee, C. F., Zweibel, E. G., Goodman, A. A., & Heiles, C. 1993, in *Protostars and Planets III*, ed. E. H. Levy & J. I. Lunine (Tuscon: Univ. Arizona Press), 327
- McKee, C. F. 1999, in *The Origin of Stars and Planetary Systems*, ed. C. J. Lada & N. D. Kylafis (Dordrecht: Kluwer), 29

- McKee, C. F., & Holliman, J. H., II 1999, *ApJ*, 522, 313
- McKee, C. F., & Tan, J. C. 2003, *ApJ*, 585, 850
- McLaughlin, D. E., & Pudritz, R. E. 1996, *ApJ*, 469, 194
- Mellema, G., Arthur, S. J., Henney, W. J., Ilev, I. T., & Shapiro, P. R. 2006, *ApJ*, accepted, (astro-ph/0512554)
- Mestel, L., & Spitzer, L. Jr., 1956, *MNRAS*, 116, 503
- Mouschovias, T. Ch. 1976, *ApJ*, 207, 141
- Mouschovias, T. Ch. 1976, *ApJ*, 206, 753
- Mouschovias, T. Ch. 1987, in *Physical Processes in Interstellar Clouds*, eds. G. E. Morfill & M. Scholer (Dordrecht:Reidel), 453
- Mouschovias, T. Ch. 1995, in *The Physics of the Interstellar Medium and Intergalactic Medium ASP Conference Series*, vol 80, eds. A. Ferrara, C. F. McKee, C. Heiles, & P. R. Shapiro
- Mouschovias, T. Ch., Tassis, K., & Kunz, M. W. 2006, *ApJ*, accepted, (astro-ph/0512043)
- Myers, P. C. 1983, *ApJ*, 270, 105
- Myers, P. C., & Goodman, A. A. 1988, *ApJ*, 326, L27
- Myers, P. C., & Goodman, A. A. 1988, *ApJ*, 329, 392
- Nakamura, F., Li, Z.-Y. 2005, *ApJ*, 631, 411
- Nakano, T., & Nakamura, T. 1978, *PASJ*, 30, 671
- Ogino, S., Tomisaka, K. & Nakamura, F., 1999, *PASJ*, 51, 637
- Ossenkopf, V., & Mac Low, 2002, *A&A*, 390, 307
- Ostriker, E. C., Gammie, C. F. & Stone, J. M. 1999, *ApJ*, 513, 259
- Padoan, P. 1995, *MNRAS*, 277, 377
- Padoan, P., Juvela, M., Goodman, A. A., & Nordlund, A. 2001, *ApJ*, 553, 227
- Padoan, P., & Nordlund, A. 2002, *ApJ*, 576, 870
- Padoan, P., & Nordlund, A. 2004, *ApJ*, 617, 559
- Palla, F., & Stahler, S. W. 1999, *ApJ*, 525, 772
- Parker, E. N. 1979, *Cosmical Magnetic Fields. Their Origin and Their Activity* (Oxford:Oxford Univ. Press)
- Pavlovski, G., Smith, M. D., & Mac Low, M.-M., 2006, *MNRAS*, 368, 943
- Piontek, R. A., & Ostriker, E. C. 2005, *ApJ*, 629, 849
- Plume, R., Jaffe, D. T., Evans, N. J. II, Martin-Pintado, J., & Gomez-Gonzalez, J. 1997, *ApJ*, 476, 730
- Racca, G., Gómez, M., & Kenyon, S. J. 2002, *AJ*, 124, 2178
- Redman, M. P., Keto, E., & Rawlings, J. M. C. 2006, *MNRAS*, accepted, (astro-ph/0604056)
- Rosolowsky, E., & Blitz, L. 2005, *ApJ*, 623, 826
- Sarma, A. P., Troland, T. H., Roberts, D. A., & Crutcher, R. M. 2000, *ApJ*, 533, 271
- Sasao, T. 1973, *PASJ*, 25, 1
- Selwood, J. A., & Balbus, S. A. 1999, *ApJ*, 511, 660
- Shadmehri, M., Vázquez-Semadeni, E., & Ballesteros-Paredes, J. 2002, in *Seeing Through the Dust : The detection of H I and the Exploration of the ISM in Galaxies*, eds. A. R. Taylor, T. L. Landecker, & A. G. Willis (San Francisco: ASP), 190
- Shirley, Y. L., Evans, N. J., II, & Rawlings, J. M. C. 2002, *ApJ*, 575, 337
- Shirley, Y. L., Evans, N. J., II, Rawlings, J. M. C., & Gregersen, E. M. 2000, *ApJS*, 131, 249
- Shu, F. H., Adams, F. C., & Lizano, S. 1987, *ARA&A*, 25, 23
- Simon, R., Jackson, J. M., Clemens, D. P., & Bania, T. M. 2001, *ApJ*, 551, 747
- Smith, M. D., Mac Low, M.-M., & Heitsch, F. 2000, *A&A*, 362, 333
- Solomon, P., Rivolo, A., Barrett, A., & Yahil, A. 1987, *ApJ*, 319, 730
- Stanimirović S. & Lazarian A. 2001, *ApJ*, 551, 53
- Steinacker, J., Lang, B., Burkert, A., Bacmann, A., & Henning, T. 2004, *ApJ*, 615, L157
- Stone, J. M., Ostriker, E. C., & Gammie, C. F. 1998, *ApJ*, 508, L99
- Strittmatter, P. A. 1966, *MNRAS*, 132, 359
- Swift, J. J., Welch, W. J., Di Francesco, J., & Stojimirovic, I. 2006, *ApJ*, 637, 392
- Tachihara, K., Mizuno, A., & Fukui, Y. 2000, *ApJ*, 528, 817
- Tachihara, K., Onishi, T., Mizuno, A., & Fukui, Y. 2002, *A&A*, 385, 909
- Tilley, D. A., & Pudritz, R. E. 2004, *MNRAS*, 353, 769
- Tilley, D. A., & Pudritz, R. E. 2006, *MNRAS*, submitted, (astro-ph/0508562)
- Truelove, J. K., Klein, R. I., McKee, C. F., Hillman II, J. H., Howell, L. H., & Greenough, J. A. 1997, *ApJ*, 489, L179
- Vázquez-Semadeni, E., & Gazol, A. 1995, *A&A*, 303, 204
- Vázquez-Semadeni, E., Ostriker, E. C., Passot, T., Gammie, C. F., Stone, J. M. 2000, in *Protostars and Planets IV*, ed. V. Mannings, A. P. Boss, & S. S. Russel (Tucson: Univ. Arizona Press), 3
- Vázquez-Semadeni, E., Kim, J., Shadmehri, M., & Ballesteros-Paredes, J. 2005, *ApJ*, 618, 344
- Vázquez-Semadeni, E., Ryu, D., Passot, T., Gonzalez, R. F., & Gazol, A. 2006, *ApJ*, 643, 245
- von Weizsäcker, C. F. 1943, *Z. Astrophys*, 22, 319
- von Weizsäcker, C. F. 1951, *ApJ*, 114, 165
- Ward-Thompson, D., Motte, F., André, P., 1999, *ApJ*, *MNRAS*, 305, 143
- Ward-Thompson, D., Scott, P. F., Hills, R. E., & André, P. 1994, *MNRAS*, 268, 276
- Ward-Thompson, D., André, P., & Kirk, J. 2002, *MNRAS*, 329, 257
- Ward-Thompson, D., Nutter, D., Bontemps, S., Whitworth, A., & Attwood, R., 2006, *MNRAS*, 369, 1201
- Wada, K., Meurer, G., & Norman, C. A. 2002, *ApJ*, 577, 197
- Wada, K., & Koda, J. 2004, *MNRAS*, 349, 270
- Williams, J. P., Blitz, L., & McKee, C. F. 2000, in *Protostars and Planets IV*, ed. V. Mannings, A. Boss, & S. Russell, (Tucson: Univ. Arizona Press), p. 97
- Yonekura, Y., Dobashi, K., Mizuno, A., Ogawa, H., & Fukui, Y. 1997, *ApJS*, 110, 21
- Young, C. H., Shirley, Y. L., Evans, N. J., II, Rawlings, J. M. C. 2003, *ApJS*, 145, 111
- Zuckerman, B., & Evans II, N. J. 1974, *ApJ*, 192, L149
- Zuckerman, B., & Palmer, P. 1974, *ARA&A*, 12, 279

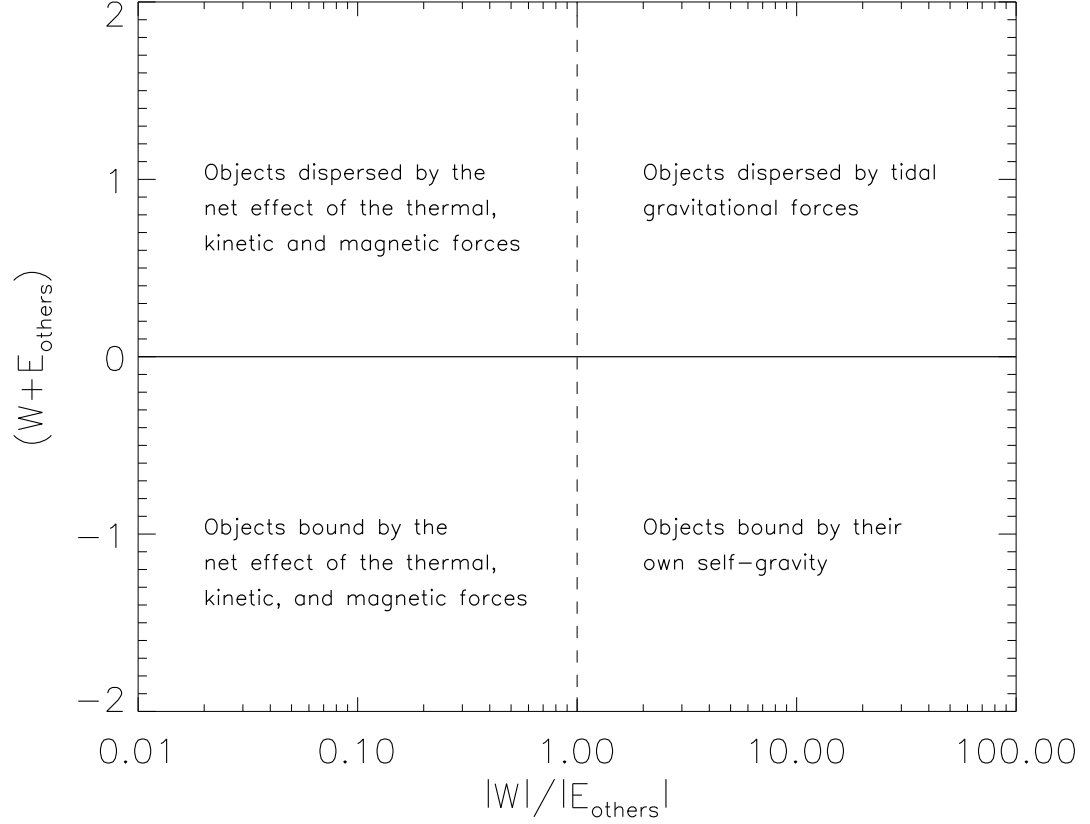


FIG. 1.— A sketch showing the gravitational boundedness state of an object as a function of the importance of its energy balance, shown here in arbitrary units. If the cloud in which the object is turbulent and magnetized, the general form of E_{other} is $E_{other} = (2(E_{th} + E_k - \tau_k - \tau_{th}) + E_m + \tau_m)$, where the E_i and τ_i (with $i = th, k, mag$) terms are the volume and surface, thermal, kinetic and magnetic energies, respectively. The detailed expression of each term is given in § 2.

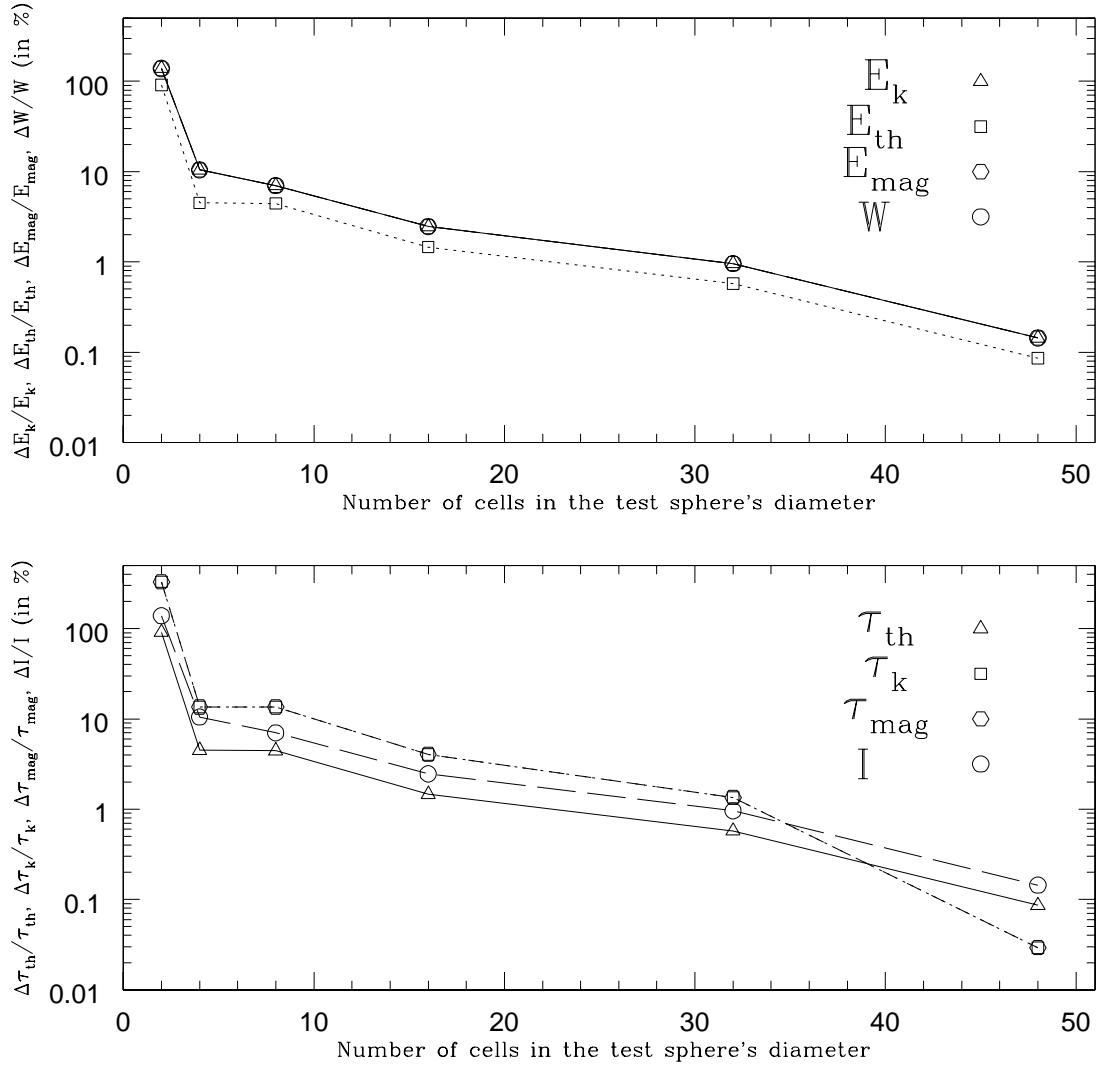


FIG. 2.— Error estimates for the terms involved in the Eulerian Virial Theorem for a test setup. The test setup is a sphere with a uniform density distribution. The velocity and magnetic fields possess, both, a pure (unphysical) radial dependence with arbitrary amplitudes which facilitates the comparison to the analytical solution. E_k , E_{th} and E_{mag} are the volume kinetic, thermal, and magnetic energy, respectively. τ_k , τ_{th} , and τ_{mag} are the surface.

TABLE 1
 NUMBER OF CLUMPS AND CORES FOUND IN THE SIMULATIONS FOR THE VARIOUS DENSITY THRESHOLDS AT SELECTED TIME-STEPS. (*, DUE TO THE LARGE NUMBER OF CELLS FOUND IN DENSE STRUCTURES IN THE NON-MAGNETIC RUN M10J4 β inf, THE LOWEST DENSITY THRESHOLD USED IN $10 \bar{n}$).

Model	time-step	$n_{thr} = 7.5 \bar{n}$	$n_{thr} = 15 \bar{n}$	$n_{thr} = 30 \bar{n}$	$n_{thr} = 60 \bar{n}$	$n_{thr} = 100 \bar{n}$	$n_{thr} = 500 \bar{n}$
M10J4 β .01	223	11	8	2	1	1	0
M10J4 β .1	30	19	18	8	5	4	0
	40	16	11	7	3	2	0
	50	14	14	9	2	1	1
	210	12	9	9	4	3	2
M10J4 β 1	20	16	14	7	2	2	0
	30	11	11	9	5	3	0
	40	15	13	8	6	1	0
	50	14	10	5	3	3	1
	60	16	15	5	4	3	1
	70	15	12	7	5	3	1
M10J4 β inf	20	23*	23	23	15	3	1
	30	19*	19	19	12	12	5
	40	22*	22	22	18	12	6

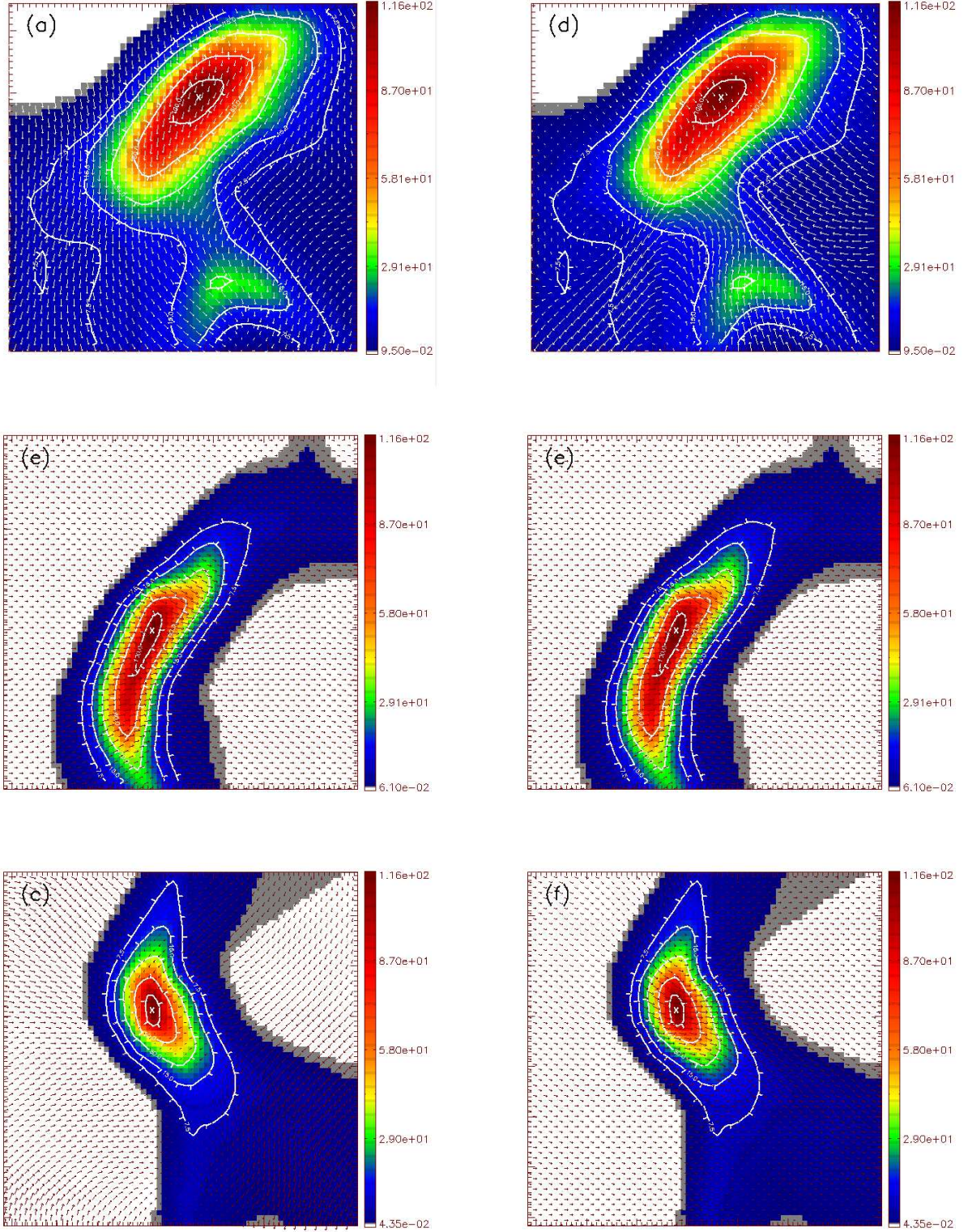


FIG. 3.— Density cut in the x (top), y (middle) and z (bottom) directions at the position of the density maximum for the densest clumps in run M10J4 β .01 at $t = 223$. This object corresponds to clump 1, 12, 20, 22 and 23 in Tab. 1. The contours show the boundary of the object for the density thresholds of 7.5, 15, 30, 60 and $100 \bar{n}$. The cross marks the position of the density maximum. Arrows show the projected velocity (left) and magnetic (right) field at the position of the two-dimensional cut, scaled to the maximum value on the grid. In order to better highlight the structure of the cloud, the resolution of the map has been artificially multiplied by a factor 2 and the map smoothed.

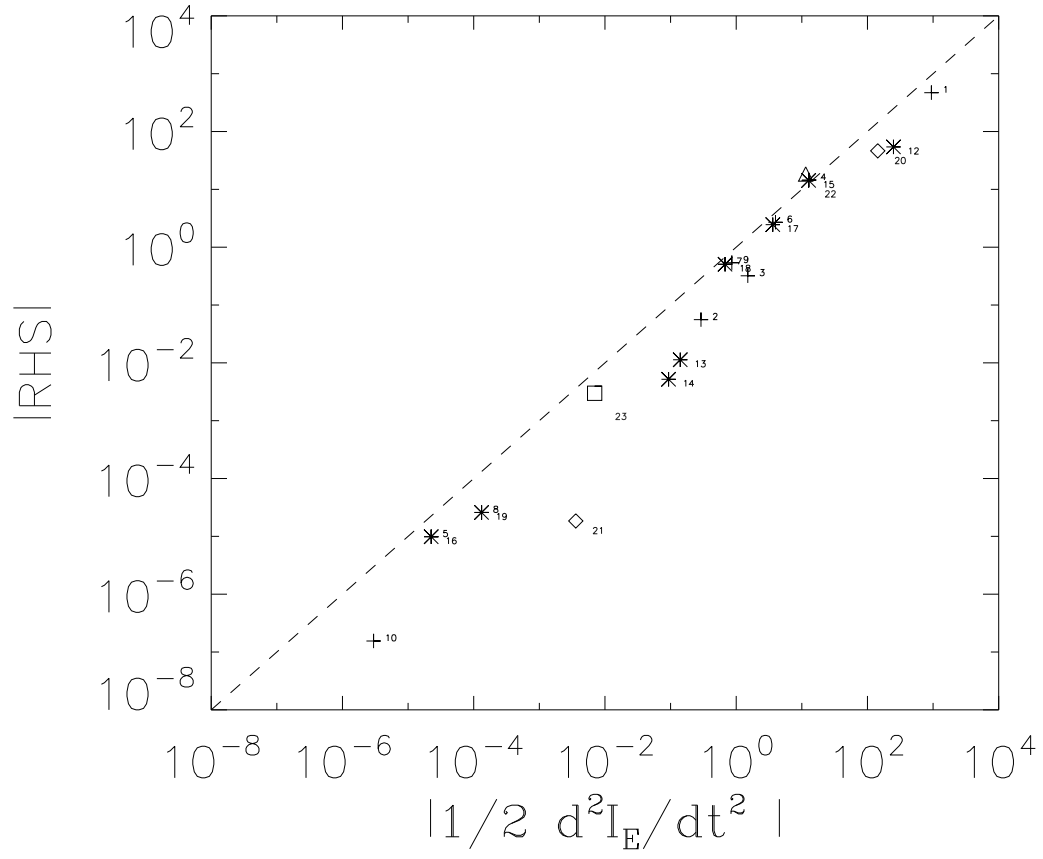


FIG. 4.— Right Hand Side terms in Eq. 1 (RHS) vs. the Eulerian second time derivative of the moment of Inertia $d^2 I/dt^2$ in run M10J4 β .01 at $t = 223 = 8.92$ Myr. The virial theorem is verified to within ~ 0.5 dex for the largest clouds. For the smaller clumps (i.e., with small numbers of cells), the larger scatter is due on the one hand to the effects of the turbulent driving, unaccounted for in Eq. 1 and by numerical noise (see Fig. 1). The $7.5 \bar{n}$ threshold level is shown with a (+), the $15 \bar{n}$ with a (*), the $30 \bar{n}$ with a (\diamond), the $60 \bar{n}$ level with a (\triangle), and the $100 \bar{n}$ level with a (\square).

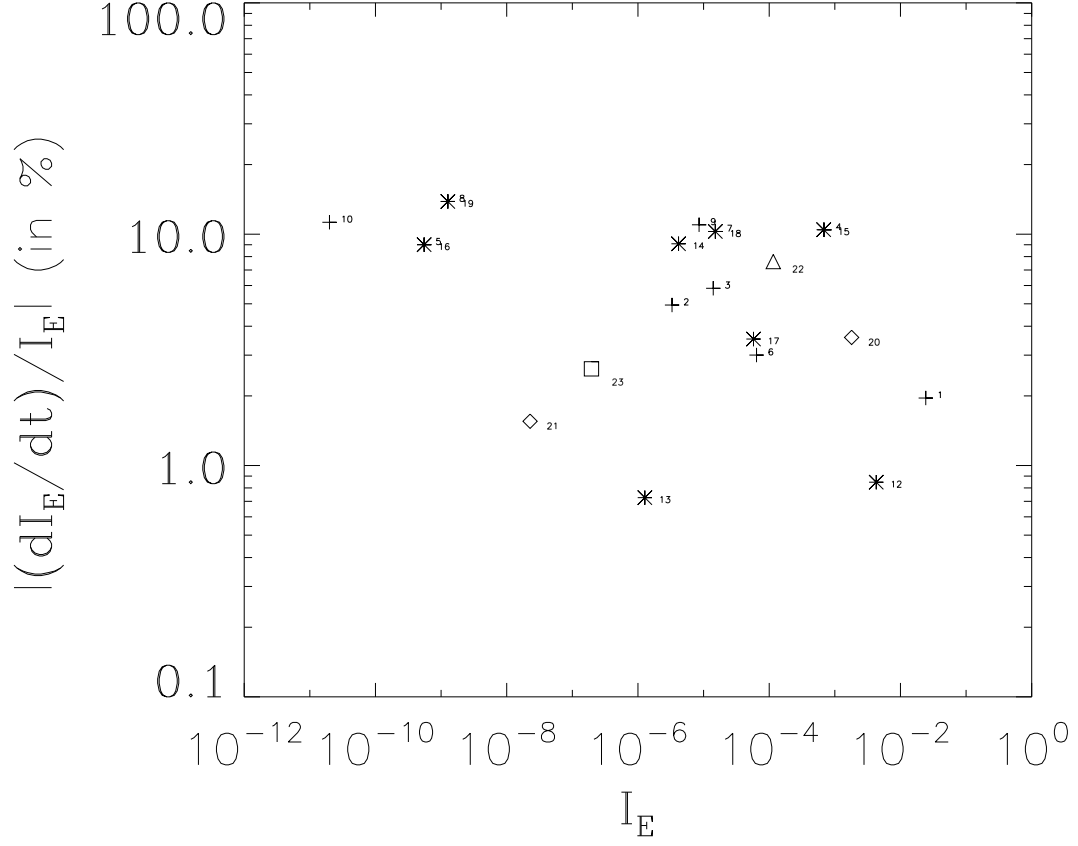


FIG. 5.— This plot shows the temporal rate of change, in percentage, of the moment of inertia for the ensemble of clumps and cores in run M10J4 β 0.01 at $t = 223 = 8.92$ Myr. The smallest clumps exhibit larger temporal variations of their moment of inertia, which is indicative of their more transient nature.

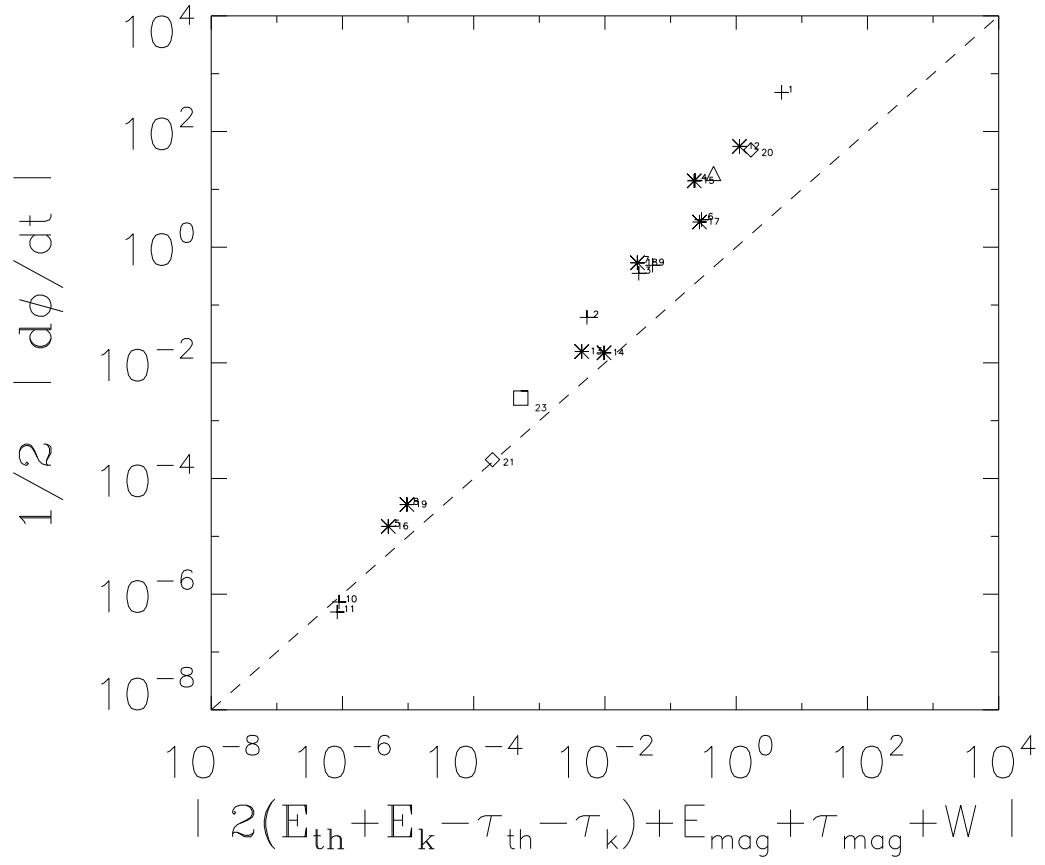


FIG. 6.— Comparison of the temporal term $d\Phi/dt$ to other terms in the RHS of the EVT. Plot is for run M10J4 β 0.01 at $t = 223 = 8.92$ Myr.

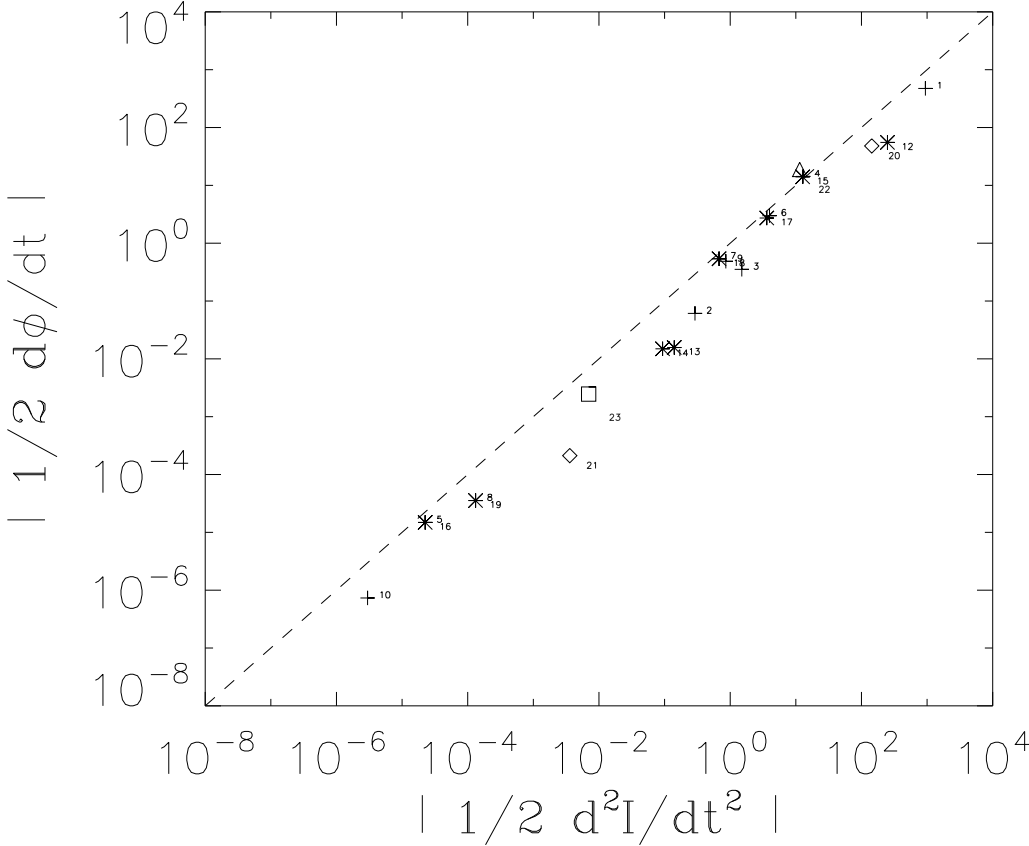


FIG. 7.— Contribution of the $d\Phi/dt$ to the total second time derivative of the moment of inertia. Plot is for run M10J4 β 0.01 at $t = 223$.

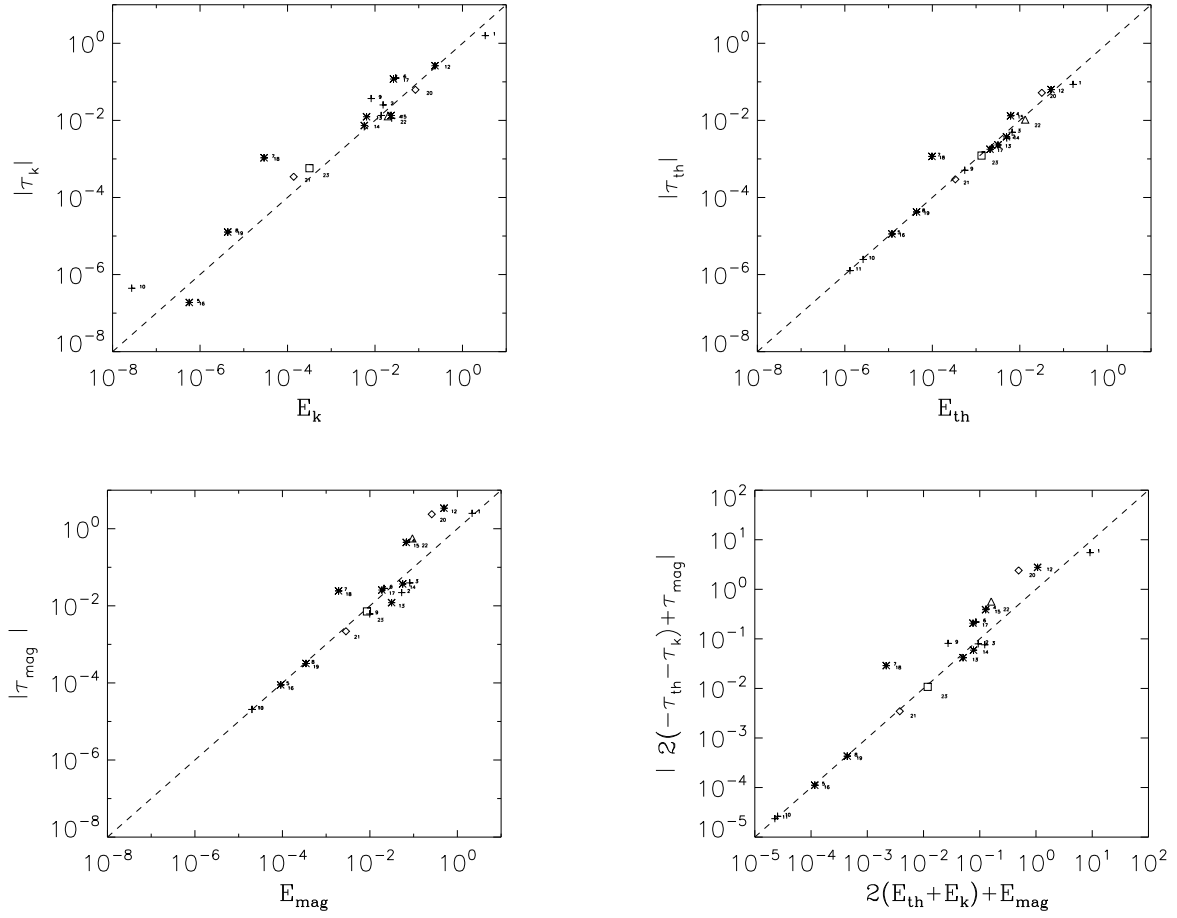


FIG. 8.— Surface energy terms versus volume energy terms a) kinetic, b) thermal, c) magnetic and d), total for run M10J4.01 at $t = 223 = 8.92$ Myr.

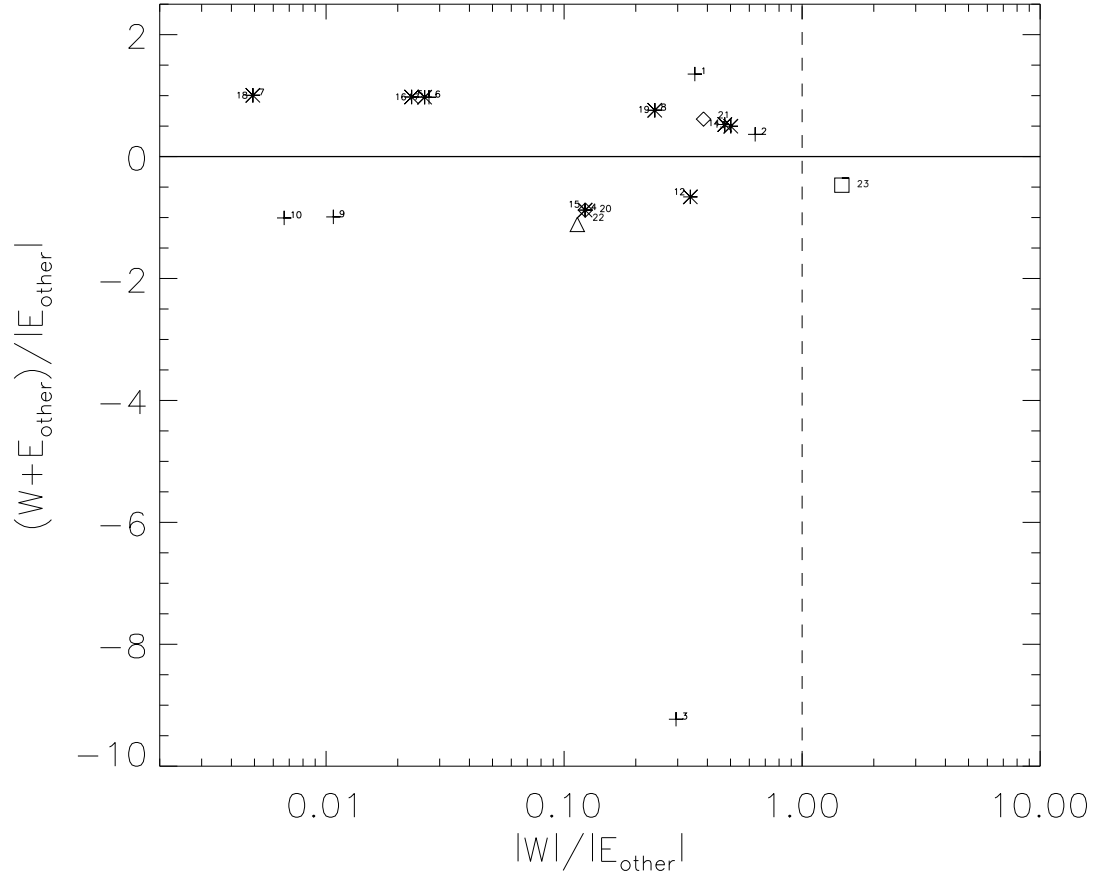


FIG. 9.— This plot compares the importance of the gravitational term $|W|$ (y axis) to the net amount of thermal, kinetic, and magnetic energies that appear in the EVT (x axis) in run M10J4 β 0.01 at $t = 223 = 8.92$ Myr.

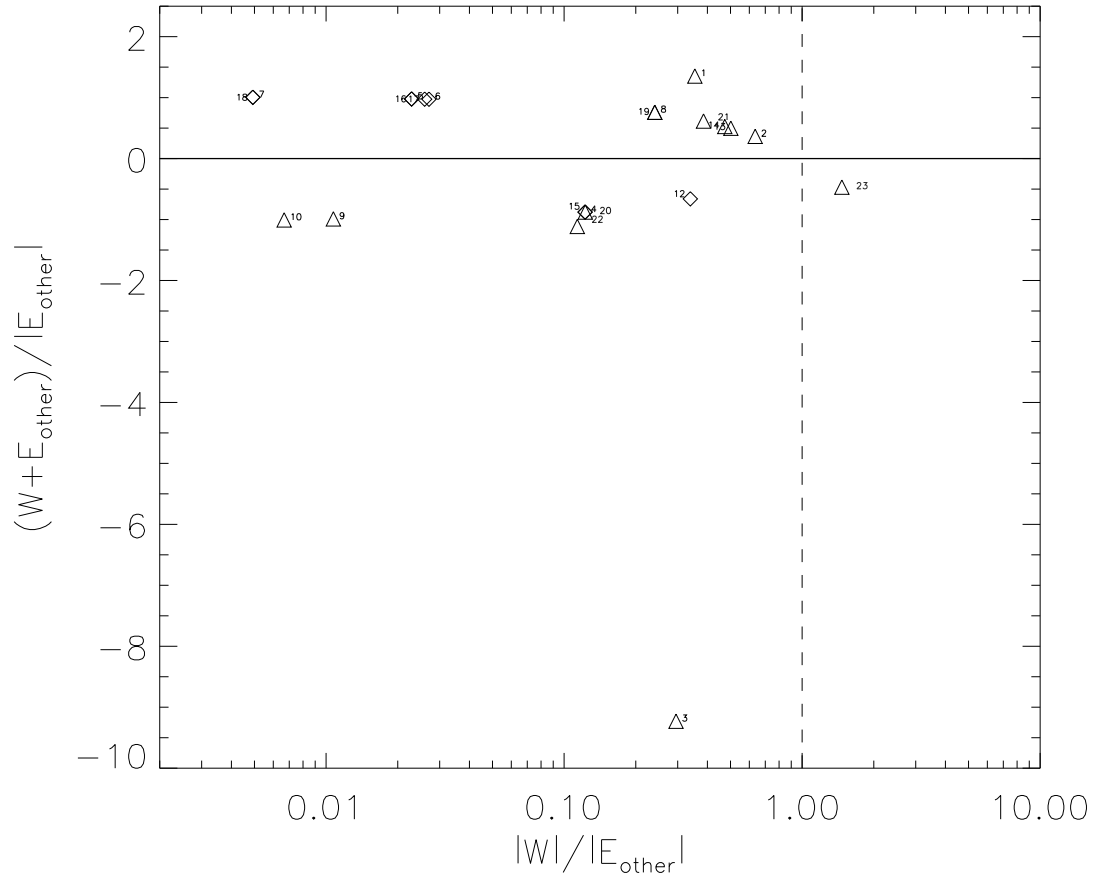


FIG. 10.— Same as Fig. 8 but where clumps are cataloged by whether they have $\tau_k > 0$ (triangles) or $\tau_k < 0$ (diamonds). A positive (i.e., negative) τ_k is indicative that the clump or core is threaded by compressive (i.e., dispersive) flows across its boundaries.

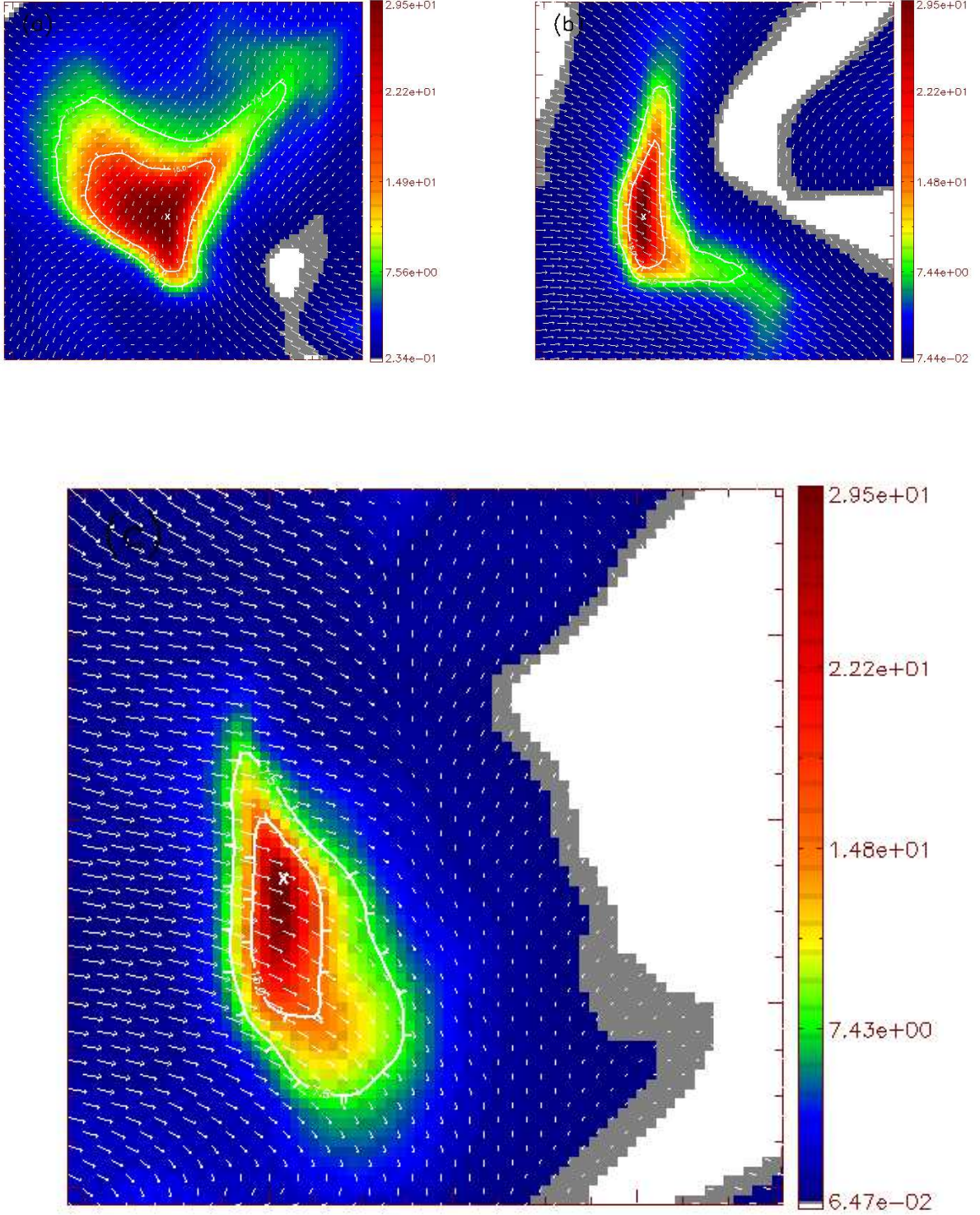


FIG. 11.— Density cuts in the x (top), y (middle), and z (bottom) directions at the position of peak density for the condensation corresponding to clumps number 3 and 14 in run M10J4 β .01 at $t = 223 = 8.85$ Myr, defined at $n_{th} = 7.5 \bar{n}$ and $15 \bar{n}$, respectively. Arrows represent the projected velocity field. In order to better highlight the structure of the cloud, the resolution of the map has been artificially multiplied by a factor 3 and the map smoothed.

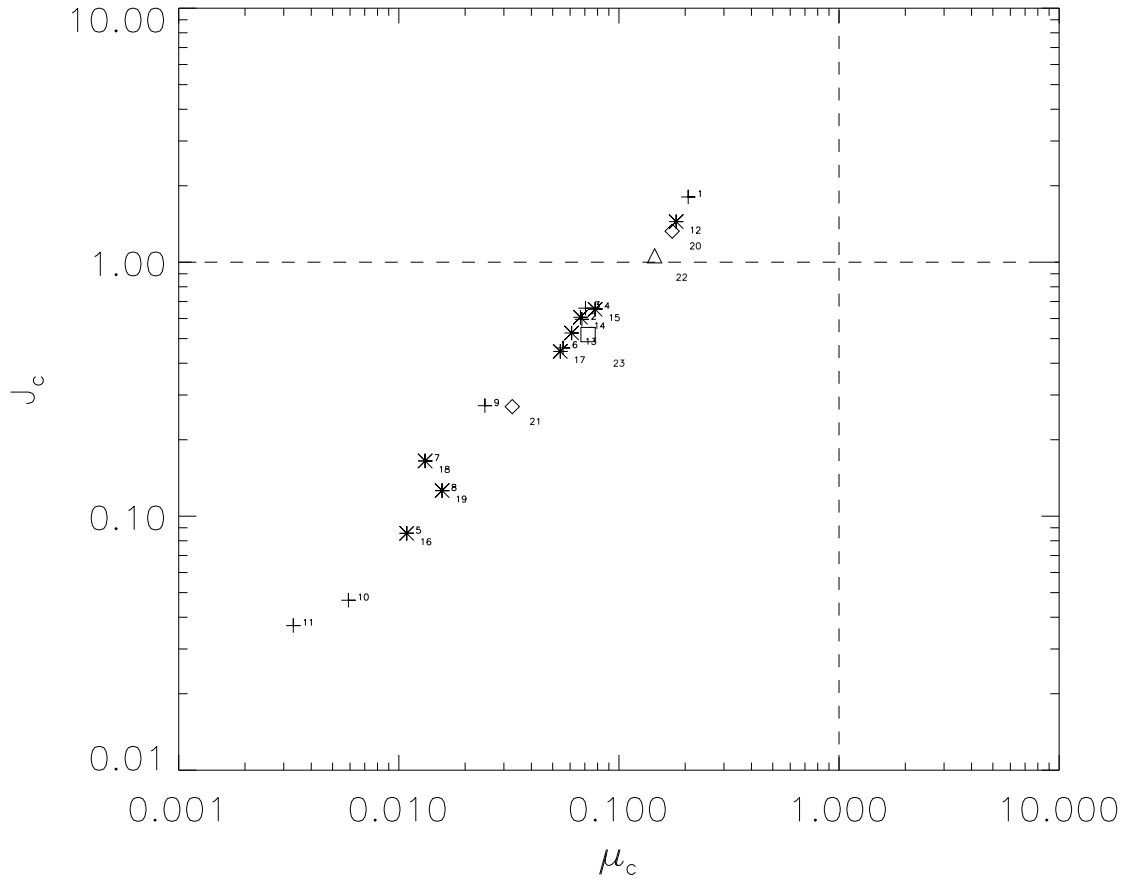


FIG. 12.— Jeans numbers J_c and mass-to-magnetic flux ratio (normalized to the critical value for collapse) μ_c of the ensemble of clumps and cores found in run M10J4 β .01 at $t = 223 = 8.92$ Myr.

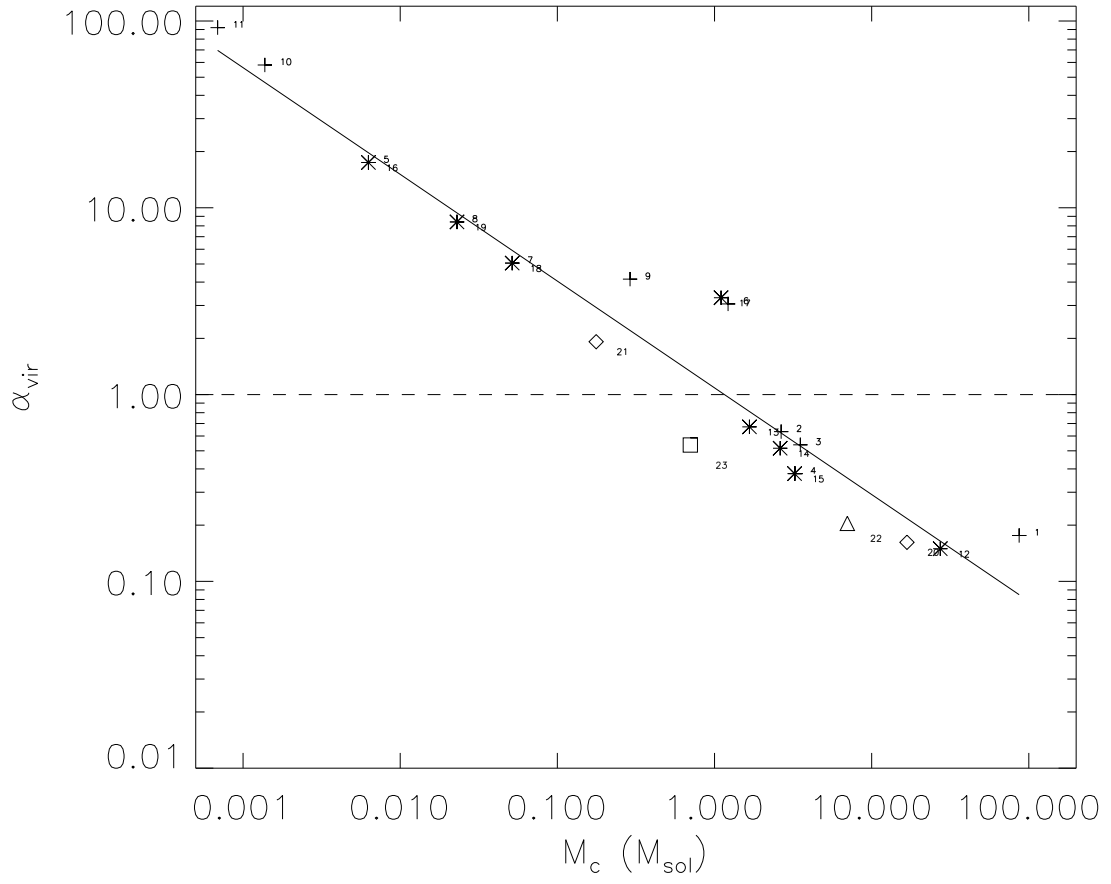


FIG. 13.— The virial parameter as a function of the masses of the clumps and cores in run M10J4 β .01 at $t = 223 = 8.92$ Myr.

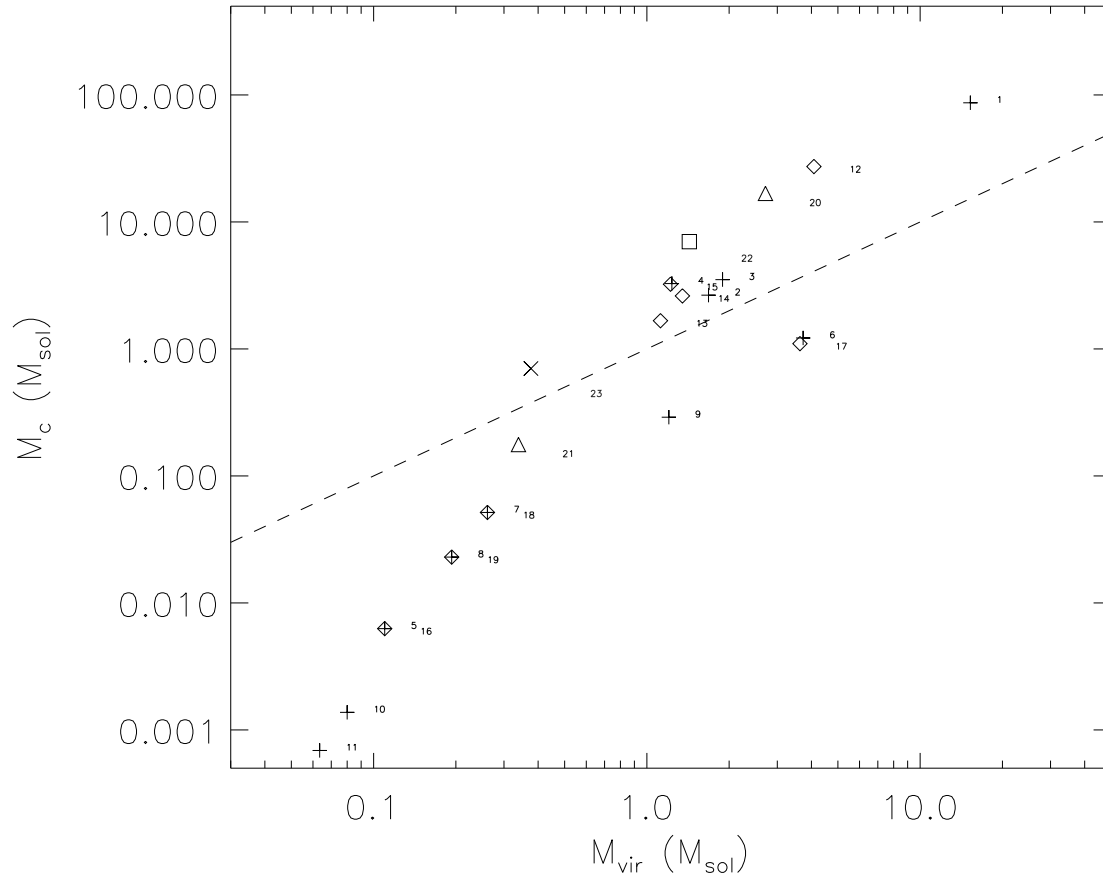


FIG. 14.— The real clumps and cores mass M_c is compared to the virial mass M_{vir} which is calculated by assuming equality between the clumps gravity and kinetic+thermal energies in run M10J4 β .01 at $t = 223 = 8.92$ Myr.

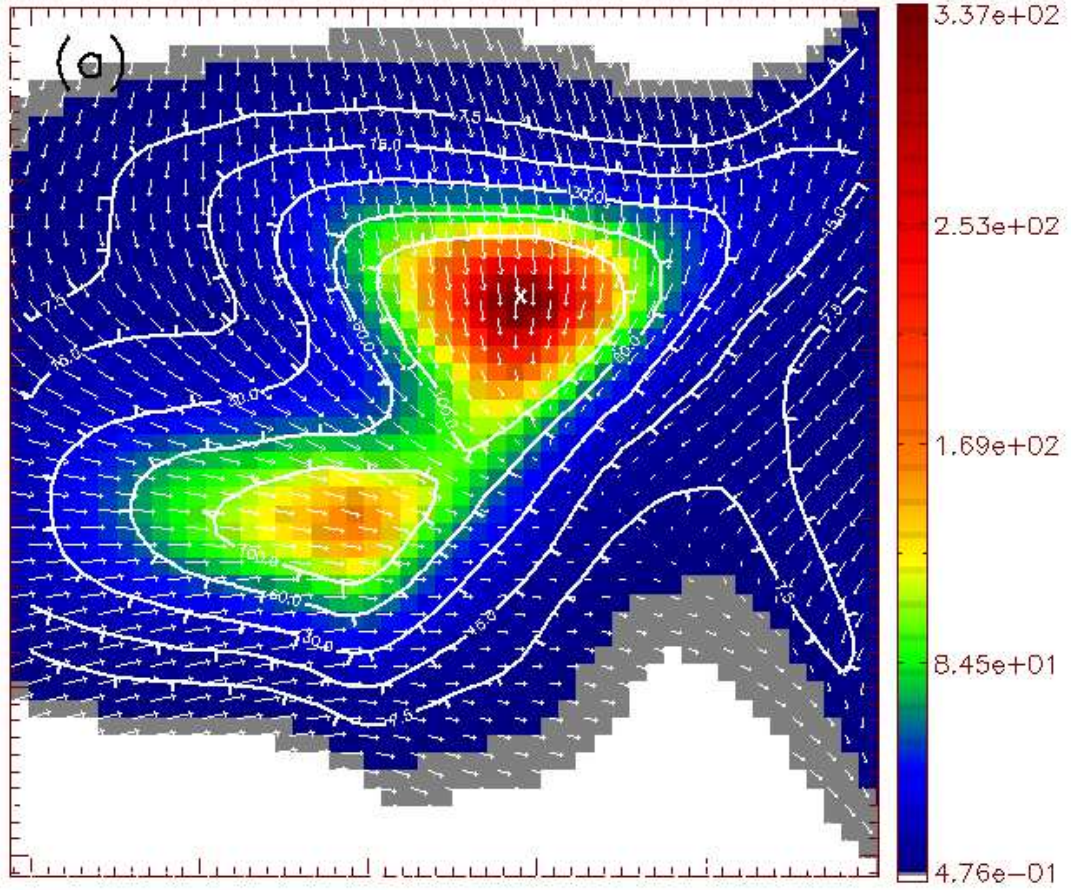


FIG. 15.— Density cut in the x-direction showing two merging core cores in run M10J4 β .1 at $t = 40 = 1.6$ Myr, respectively. Arrows represent the projected velocity field.

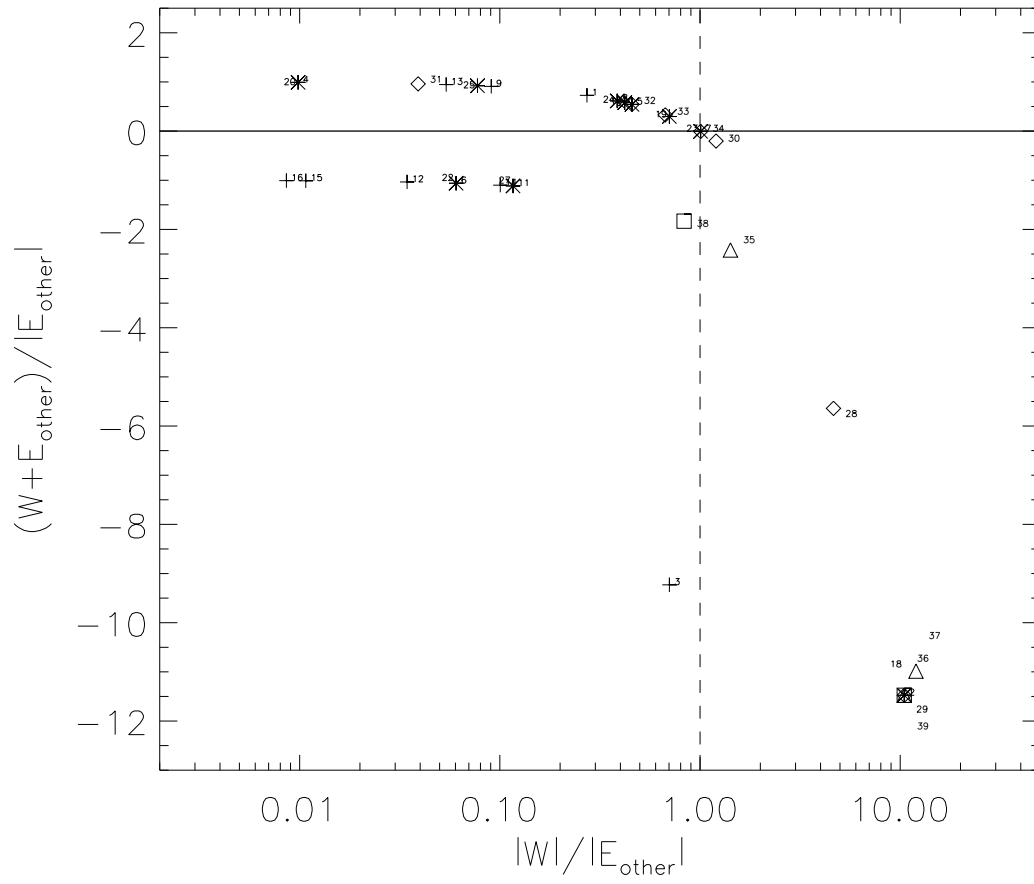


FIG. 16.— Same as Fig. 8 but for the moderately supercritical run M10J4 β .1 at $t = 40 = 1.6$ Myr.

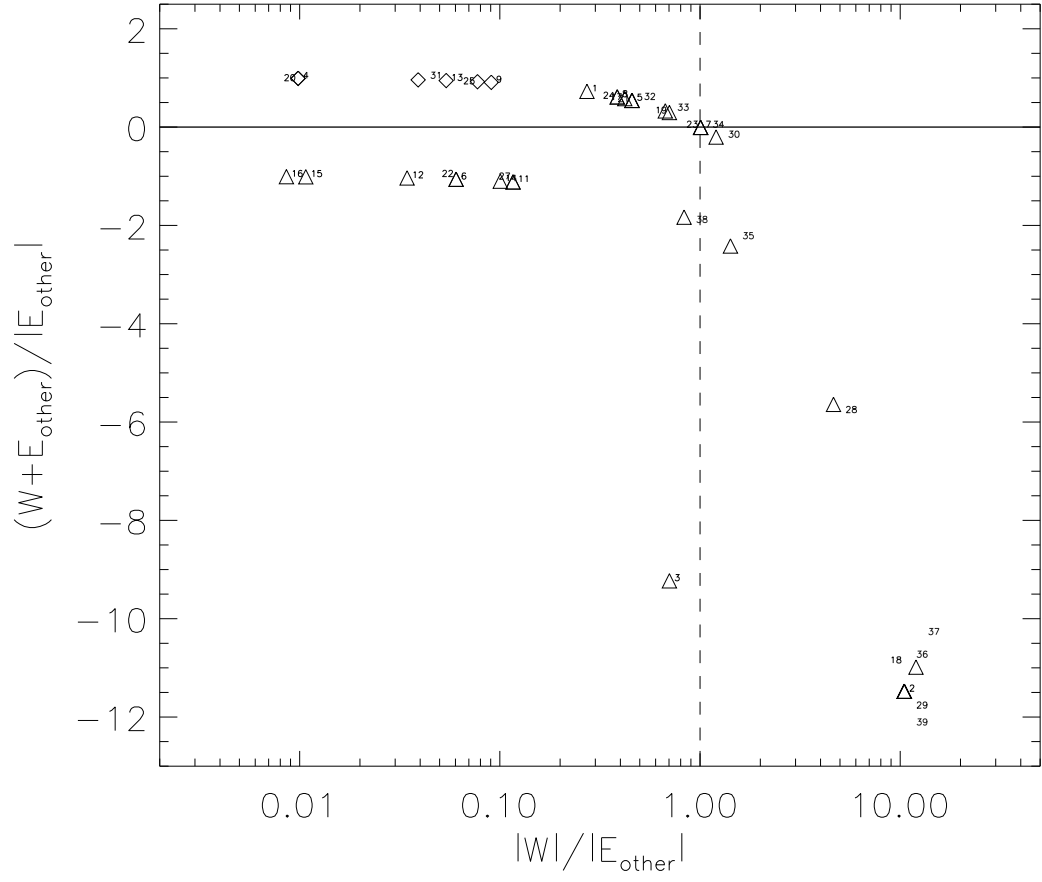


FIG. 17.— Same as Fig. 9 but for the moderately supercritical run M10J4 β .1 at $t = 40 = 1.6$ Myr.

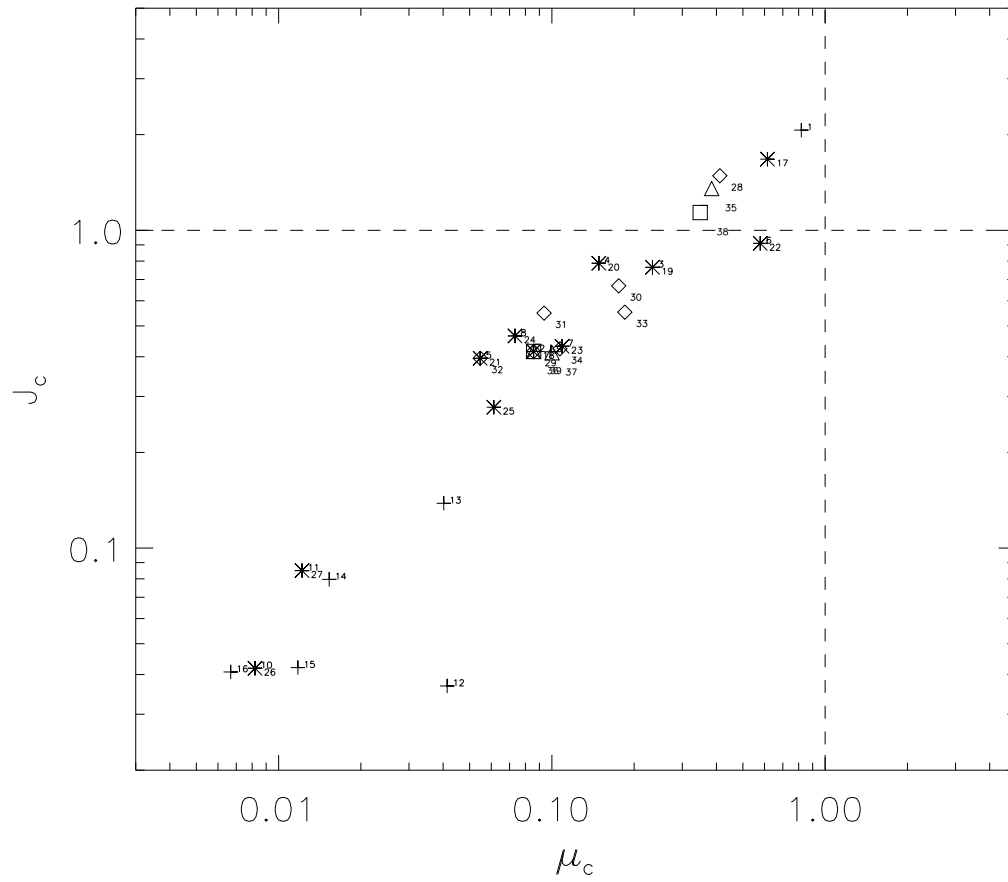


FIG. 18.— Jeans numbers J_c and mass-to-magnetic flux ratio (normalized to the critical value for collapse) μ_c of the ensemble of clumps and cores found in the moderately supercritical run M10J4 β .1 at $t = 40 = 1.6$ Myr.

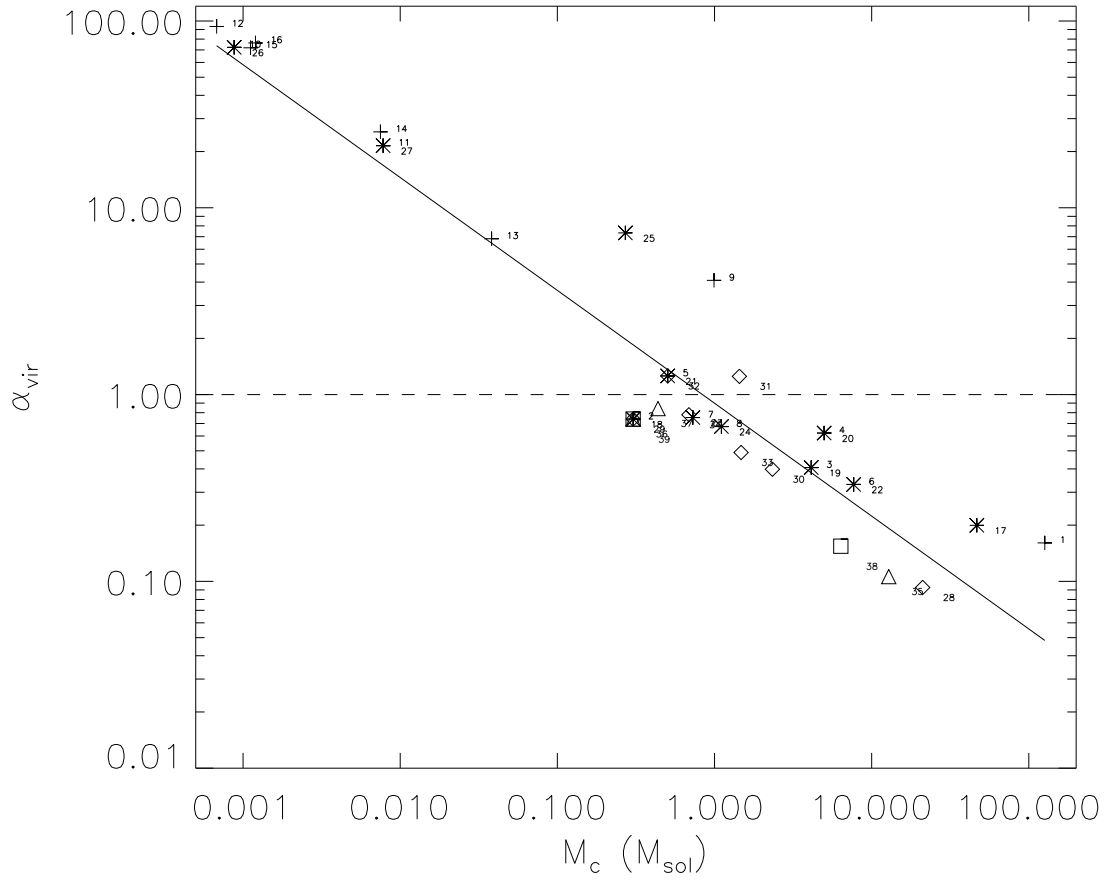


FIG. 19.— Same as Fig. 13 but for run M10J4/ β .1 at $t = 40 = 1.6$ Myr.

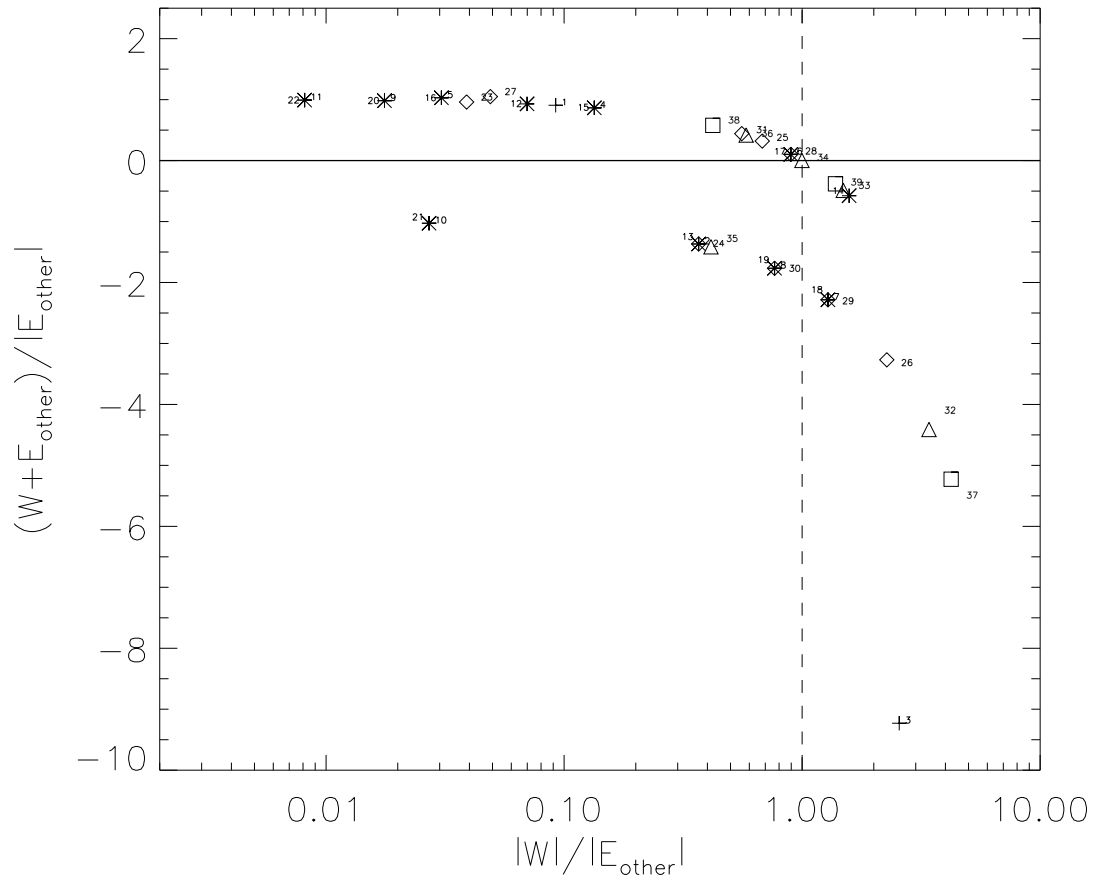


FIG. 20.— Same as Fig. 9 but for the strongly supercritical run M10J4 β 1 at $t = 30 = 1.2$ Myr.

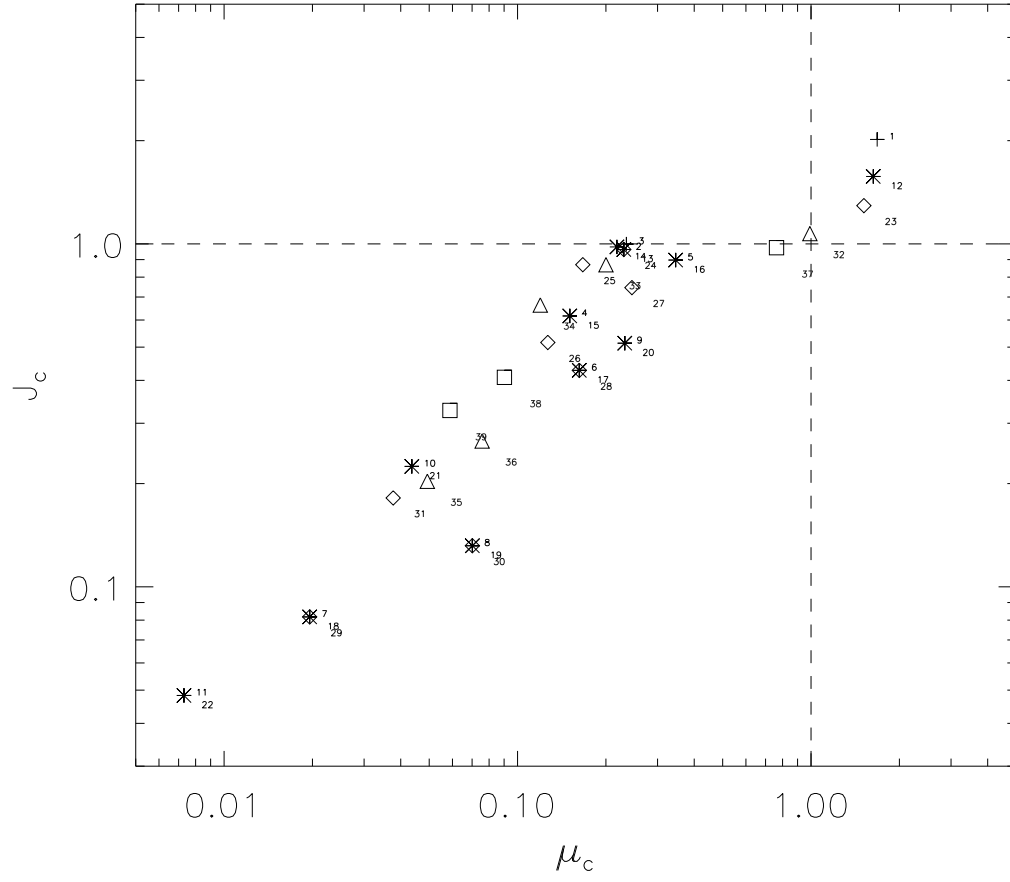


FIG. 21.— Same as Fig. 12 but for the strongly supercritical run M10J4 β 1 at $t = 30 = 1.2$ Myr.

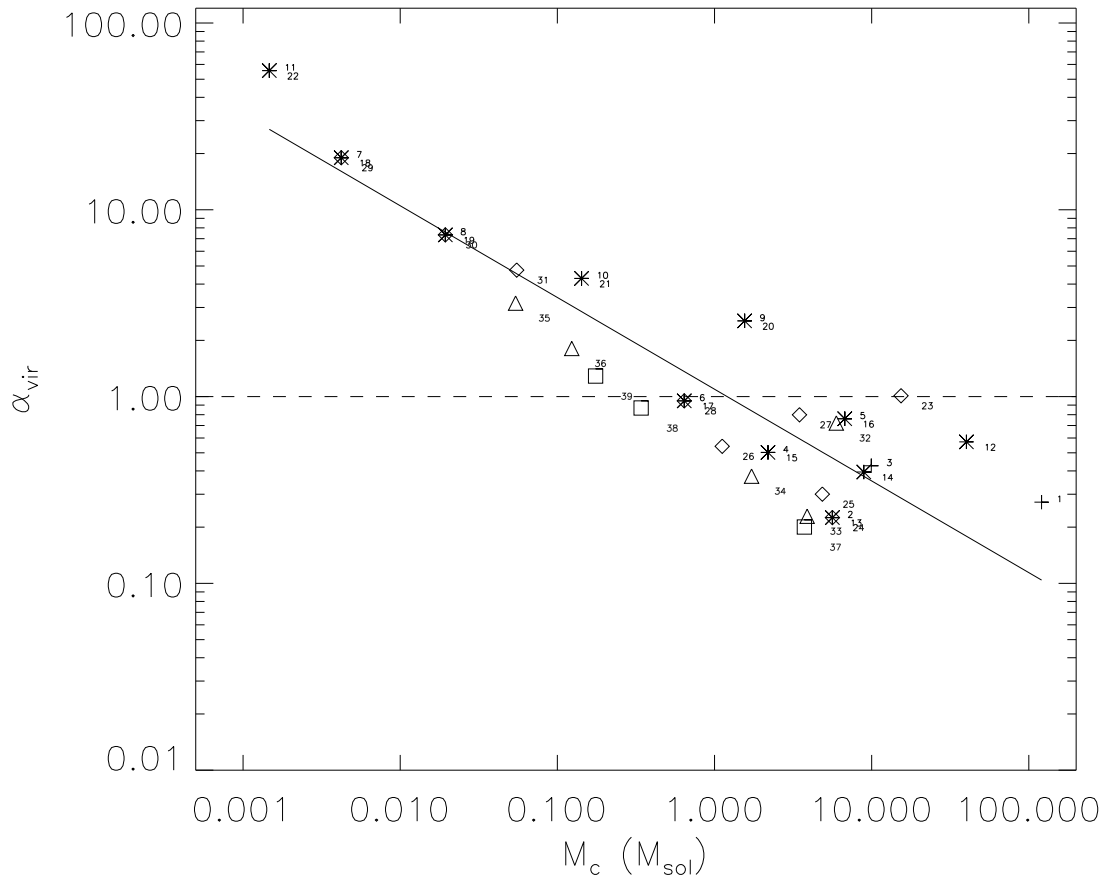


FIG. 22.— Same as Fig. 13 but for the strongly supercritical run M10J4 β 1 at $t = 30 = 1.2$ Myr.

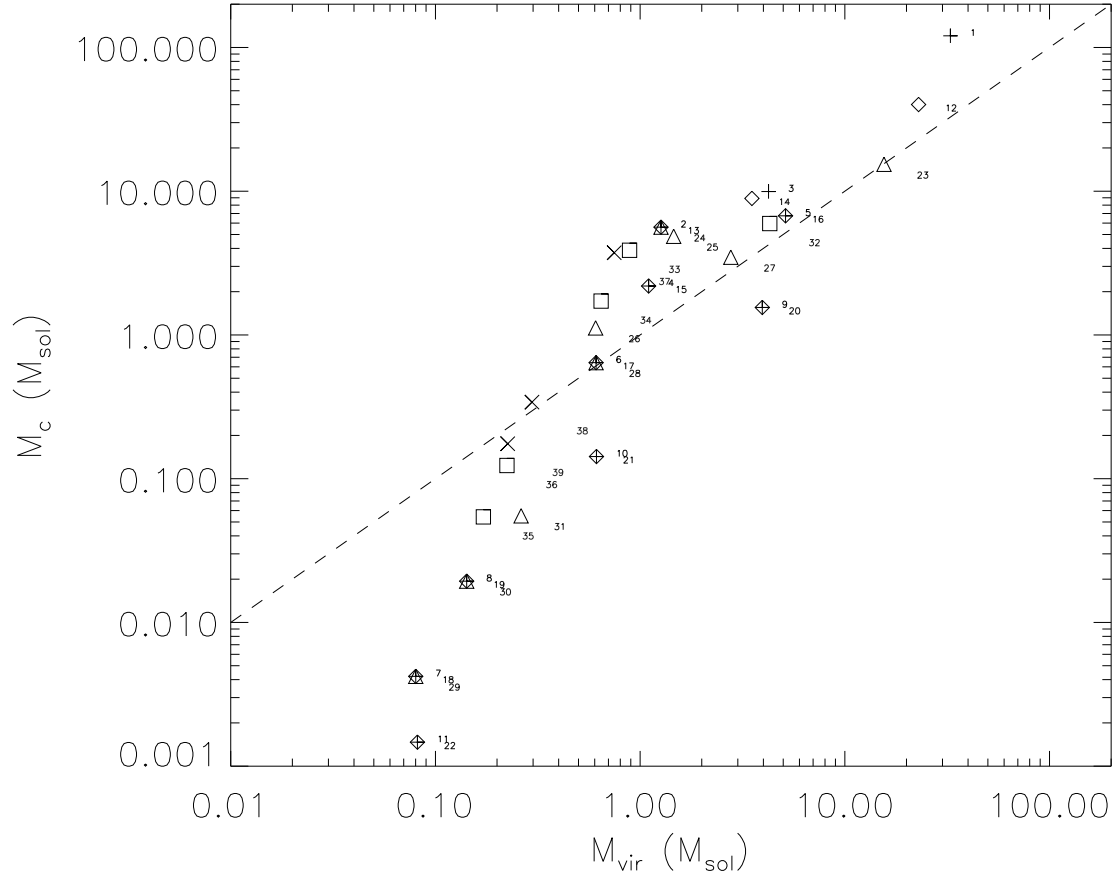


FIG. 23.— Same as Fig. 14 but for the strongly supercritical run M10J4 β 1 at $t = 30 = 1.2$ Myr.

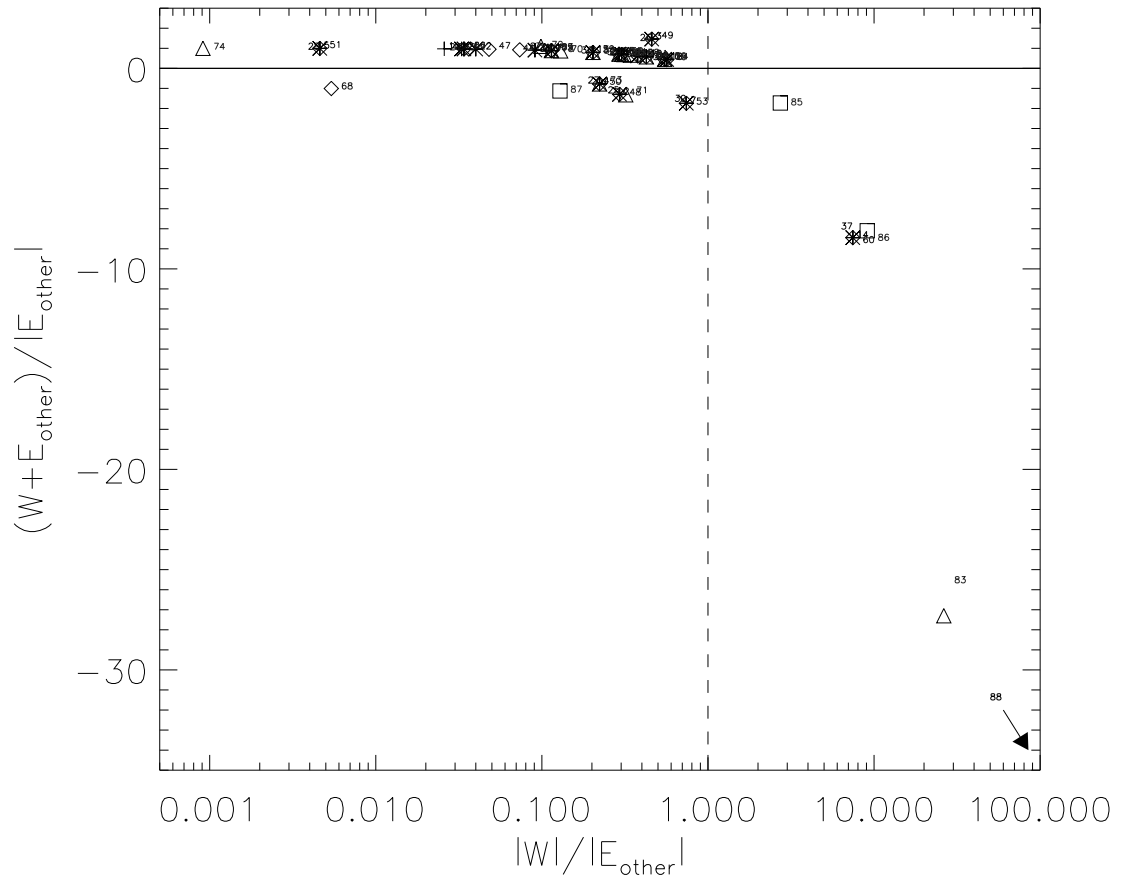


FIG. 24.— Same as Fig. 9 but for the non-magnetic run M10J4 β inf at $t = 20 = 0.8$ Myr.

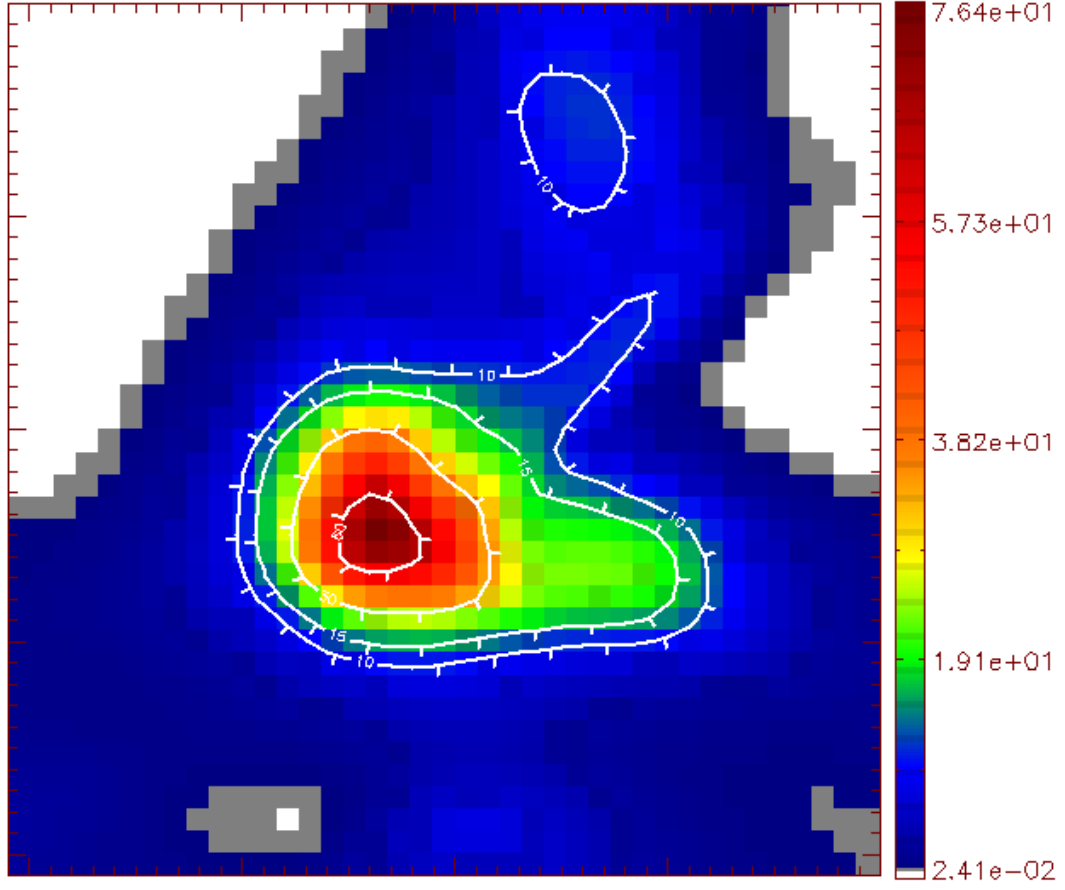


FIG. 25.— Cut at the position of the density maximum in the x-direction of the box for the object corresponding to clumps (14,37,60, and 83 at the thresholds levels of 10,15,30 and $60 \bar{n}$, respectively) in the non-magnetic run M10J4 β inf at $t = 20 = 0.8$ Myr. The dynamical and thermodynamical properties as well as the bean-like morphology of this object resemble those of the starless core Barnard 68 (Alves et al. 2001a,b). The pixel resolution has been multiplied by a factor 10 in order to better highlight the morphology of the core. In order to better highlight the structure of the cloud, the resolution of the map has been artificially multiplied by a factor 8 and the map smoothed.

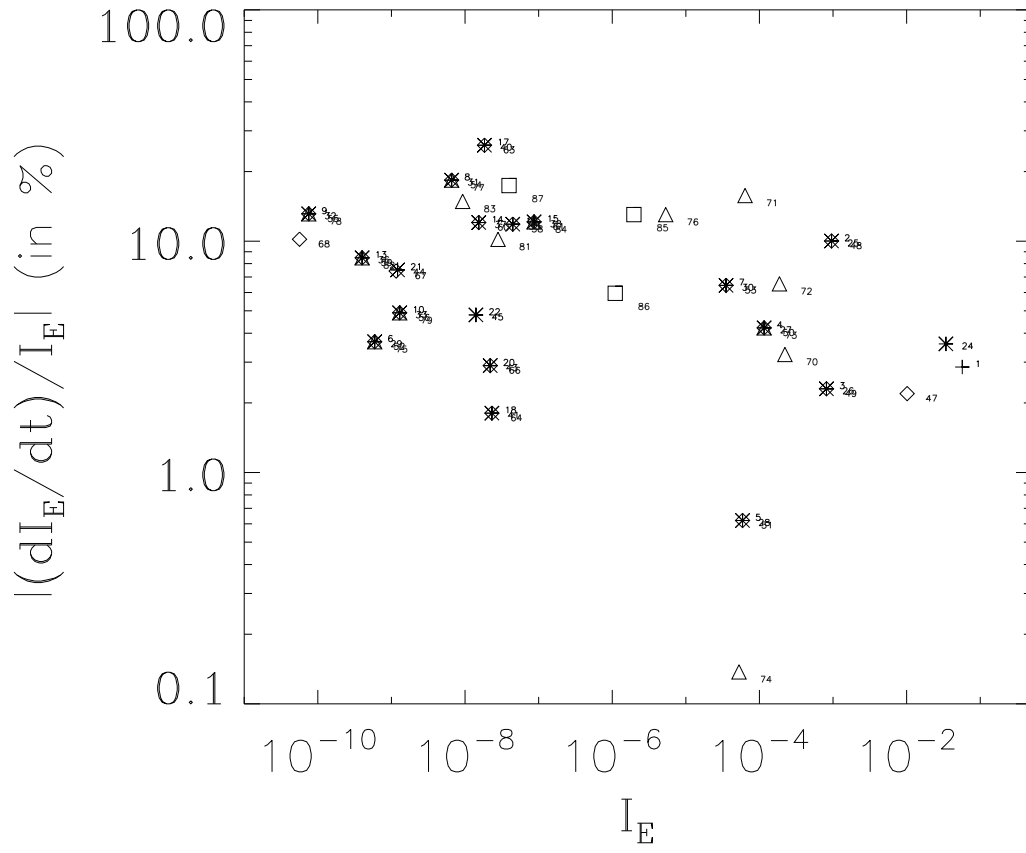


FIG. 26.— Same as Fig. 4 but for the non-magnetic run M10J4 β inf at $t = 20 = 0.8$ Myr. The Barnard 68-like object corresponding to clumps (14,37,60, and 83 at the threshold levels of 10,15,30 and 60 \bar{n}), shows a temporal rate of change of it's moment of inertia of the order of $\sim 10\%$.

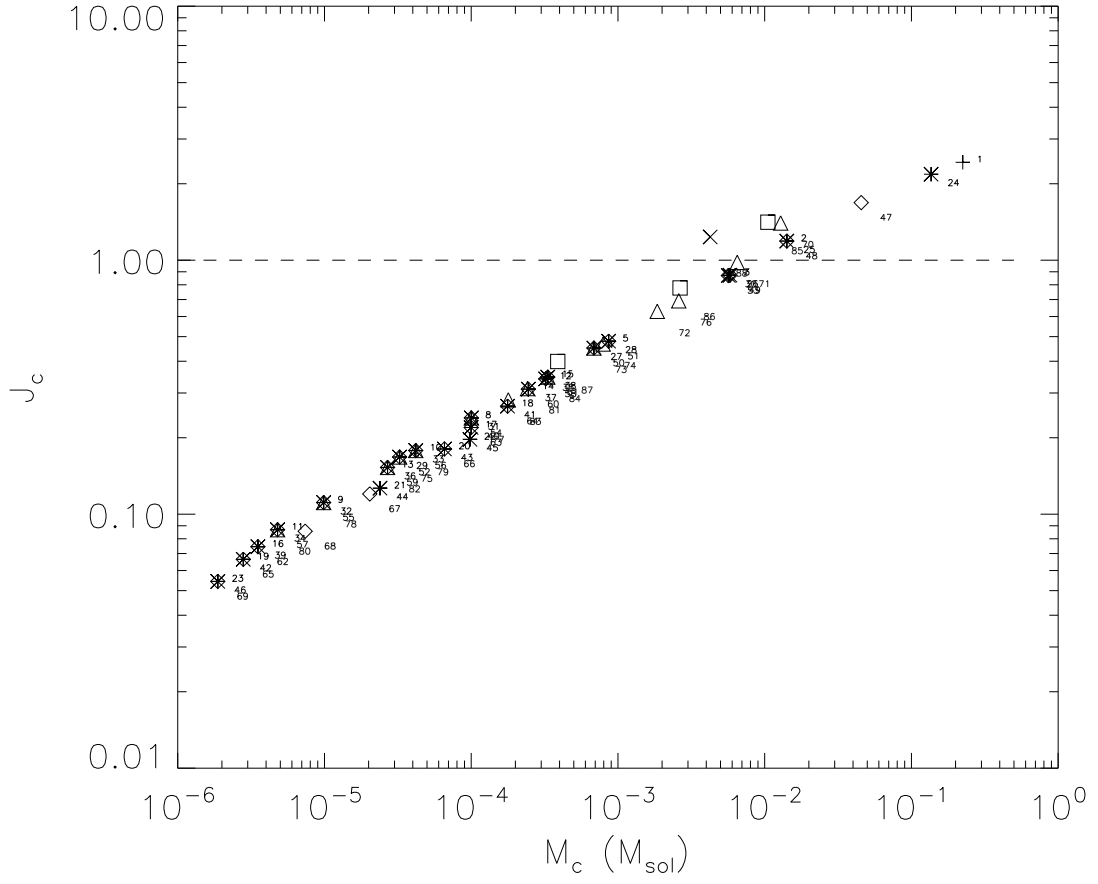


FIG. 27.— Jeans number-Mass relations for the ensemble of clumps and cores in run M10J4 β inf at $t = 20 = 0.8$ Myr.

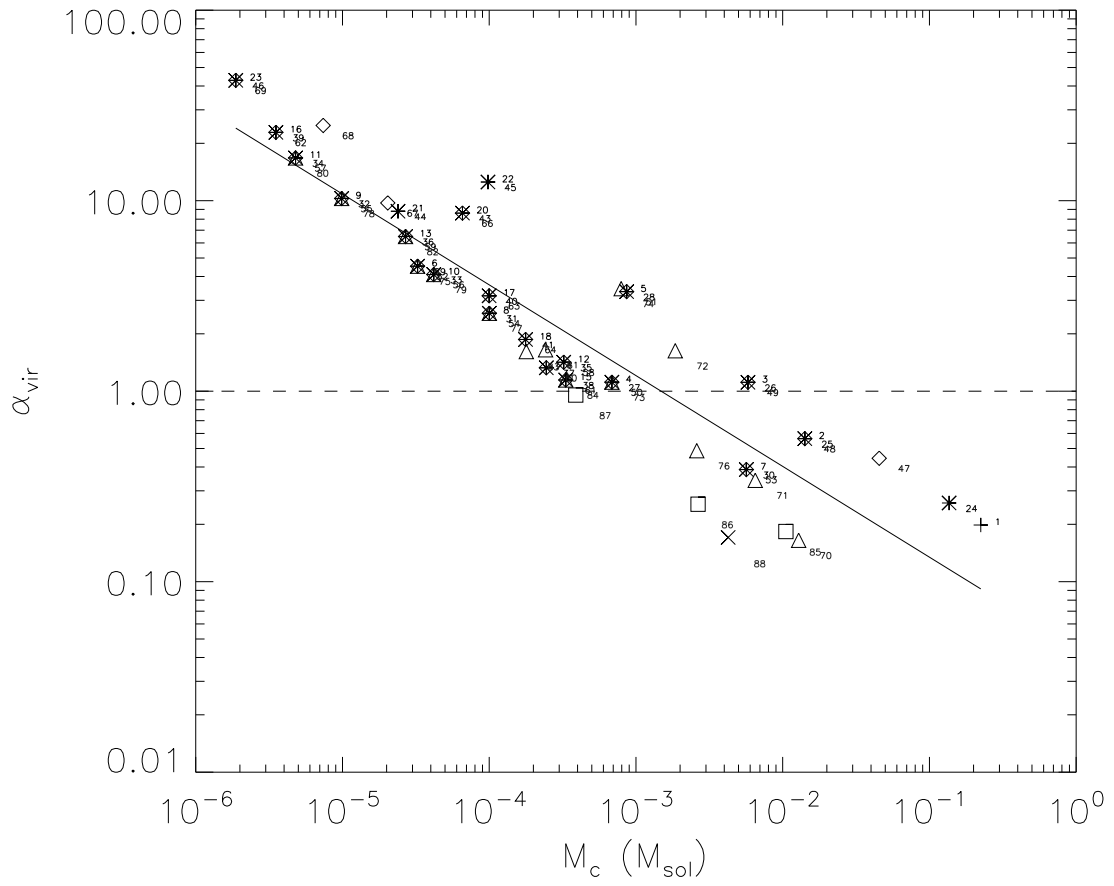


FIG. 28.— Similar to Fig. 13 but for run M10J4 β inf at $t = 20 = 0.8$ Myr.